ORIGINAL ARTICLE



Computational modeling of flow-mediated angiogenesis: Stokes–Darcy flow on a growing vessel network

Adithya Srinivasan¹ · Adrian Moure² · Hector Gomez^{1,3}

Received: 29 June 2023 / Accepted: 16 August 2023 / Published online: 17 September 2023 © The Author(s), under exclusive licence to Springer-Verlag London Ltd., part of Springer Nature 2023

Abstract

Tumor angiogenesis, the growth of new blood vessels towards a tumor, plays a critical role in cancer progression. Tumors release tumor angiogenic factors (TAF) that trigger angiogenesis upon reaching a pre-existing capillary. Although not frequently studied, the convective transport of TAF plays a key role in determining the resulting shape of the vasculature. In this work, we propose a computational method that couples an angiogenesis model with Stokes—Darcy flow to simulate the impact of flow on angiogenesis. We use the phase-field method to implicitly describe the vasculature and capture the temporally evolving interface between the intra- and extravascular flow. The implicit description of the interface eliminates the need to re-mesh the vasculature which would otherwise be required due to the movement of the interface. We propose a finite-element discretization to solve the coupled problem and illustrate the accuracy of the algorithm by comparing a numerical solution with a manufactured test case in a simplified scenario. The numerical simulations demonstrate the impact of the convective transport of TAF on the shape of the vasculature. It predicts that the vasculature network grows prominently against the flow direction and that the growth of vasculature is enhanced with increasing interstitial flow magnitude.

Keywords Angiogenesis · Phase field · Vascular flow · Stokes–Darcy

1 Introduction

During the early stages of cancer development, cancerous cells receive the required nutrition from the existing vascular network. As the tumor grows, it requires additional nutrients and oxygen which cannot be delivered by the existing capillary network. This creates hypoxic cells which release chemical signals, generically called tumor angiogenic

Hector Gomez hectorgomez@purdue.edu

Adithya Srinivasan srini162@purdue.edu

Adrian Moure amoure@caltech.edu

- School of Mechanical Engineering, Purdue University, 585 Purdue Mall, West Lafayette, IN 47907, USA
- Department of Mechanical and Civil Engineering, California Institute of Technology, 1200 E California Blvd, Pasadena, CA 91125, USA
- Weldon School of Biomedical Engineering, Purdue University, 206 S Martin Jischke Dr., West Lafayette, IN 47907, USA

factors (TAF), that trigger tumor angiogenesis [1]. Tumor angiogenesis is the growth of new capillaries in the direction of the tumor and is a critical stage in the development of cancer as it leads to increased malignancy of the tumor and metastasis [2].

In the past decades, tumor angiogenesis research has focused on the biochemical signaling pathways. In particular, a number of TAFs that promote vessel growth have been identified. However, despite its importance, the role of biophysical cues has received less attention. Recent experimental research indicates that various flow-based biophysical cues have a significant impact on angiogenesis [3–10]. The research conducted suggests that the intravascular fluid shear stress controls the location of sprouting in angiogenesis [6, 10], the growth of vasculature is biased against the direction of interstitial flow [4], and interstitial flow magnitudes affect the growth rate of vasculature [3]. Thus, the determination of intravascular and interstitial flow is key to understanding tumor angiogenesis.

Despite recent advancements in microfluidics that enable *in vitro* models of interstitial flow in micro-vascular tissues, it remains challenging to understand the complex coupling of flow and angiogenesis *in vivo*. Under certain assumptions,



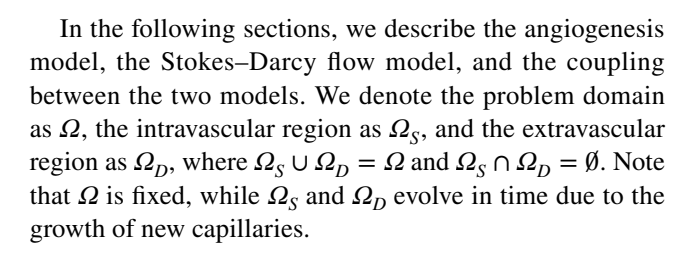
computational modeling can provide high-resolution information on fluid flow and vasculature growth, making it a promising approach to studying this problem.

Earlier computational models of flow-mediated angiogenesis have shown success using simplified flow models (see [11-14]), but they cannot perform high fidelity simulations of angiogenesis coupled with intra- and extravascular flow on a temporally evolving capillary network. Here, we propose an angiogenesis model coupled with a multiphysics flow model which uses Stokes flow and Darcy flow to represent the intra- and extravascular flow, respectively. The angiogenesis model was developed using the work of [15]. The main computational challenge in this model is that the vascular network is evolving with time due to angiogenic growth. Therefore, classical interface-tracking formulations [16] of the Stokes–Darcy problem [17] would require moving meshes that discretize the time-evolving intra- and extravascular spaces. We address this challenge using the phase-field approach, which is a mathematical modeling technique to reformulate moving boundary problems as differential equations posed on a fixed domain [18, 19].

We develop space and time discretization schemes that successfully handle the nonlinear and multiphysics nature of the problem. We show that our algorithm is second-order accurate in space using a manufactured solution for a simplified flow problem. We then show that the model naturally predicts the experimental observation that the vasculature grows prominently against the flow and that the growth of the vasculature is enhanced by increasing interstitial flow magnitude. This work opens new opportunities to understand the complex interplay between flow and vessel growth in biological systems. The algorithms developed here may also be applicable to other important engineering problems such as flow on a propagating crack embedded in a porous medium.

2 Mathematical model

We propose a flow-mediated angiogenesis model that couples capillary growth and vascular flow. We capture capillary growth with a hybrid model developed using the work of [13, 15]. We capture the intra- and extravascular flow with the Stokes–Darcy model for an incompressible fluid, where the intravascular flow is governed by the Stokes equation and the interstitial (i.e., extravascular) flow is controlled by the Darcy equation for saturated flow in porous media. The angiogenesis and flow models are fully coupled. On the one hand, flow biases the transport of TAF and, hence, the growth of new capillaries. On the other hand, continuous changes in the vascular network reshape the Stokes and Darcy domains, which modifies the fluid flow.



2.1 Angiogenesis model

We use a hybrid model similar to that described in [13, 15] to capture capillary growth. The continuous compartment of the model accounts for the vascular network and TAF dynamics, while the discrete compartment controls the evolution of tip endothelial cells (TECs). TEC motion, which is controlled by TAF gradients, drives the growth of the capillaries. The model unknowns are c(x,t) and f(x,t), which represent the vascular network and the TAF concentration, respectively, where $x \in \Omega$. We also consider the flow velocity u(x,t), which represents the Darcy flow in the interstitium and the Stokes flow in the vascular network. The flow velocity u is computed with the Stokes–Darcy flow model (see Sect. 2.2).

Continuous compartment

We resort to the phase-field method [19, 20] to capture the evolution of the capillary network. For more details on the phase-field approach, see [18]. In our model, the phase field c takes the value 1 in the intravascular region, -1 in the interstitium, and smoothly transitions between -1 and 1 across the capillary wall. The evolution of c is governed by a Cahn–Hilliard equation extended with a proliferation term, which is expressed as

$$\frac{\partial c}{\partial t} = \nabla \cdot \left[M \nabla \left(\mu(c) - \lambda^2 \Delta c \right) \right] + B(f) c H(c) \quad \text{in } \Omega, \tag{1}$$

where the constant M>0 is the mobility, λ is a parameter that represents the width of the capillary wall, H is the Heaviside function, and $\mu(c)=-c+c^3$ is the chemical potential. The first term of the right-hand side accounts for the Cahn–Hilliard dynamics of mass-conserved systems, while the second term is a proliferation term that enforces the formation of the capillary behind the advancing TEC (TEC motion is described below in this section). The proliferation function B is defined as

$$B(f) = \begin{cases} B_0 f, & \text{if } f < f_p, \\ B_0 f_p, & \text{if } f \ge f_p, \end{cases}$$
 (2)

where the constant B_0 is the proliferation rate and f_p is the TAF cut-off value for maximum proliferation.

In our model, TAF is produced by hypoxic cells that are located in the interstitium. We account for TAF diffusion, natural degradation, and uptake by the endothelial cells. We



also account for the advective transport of TAF driven by u. The evolution equation for TAF is written as

$$\frac{\partial f}{\partial t} + \nabla \cdot (\boldsymbol{u}f) = \nabla \cdot (D_0 \nabla f) + P_f (f_{\text{HYC}} - f) - U(c)f \quad \text{in } \Omega,$$
(3)

where D_0 is the TAF diffusion coefficient in the interstitium, the constant f_{HYC} represents the maximum TAF concentration inside the hypoxic cells, and the function P_f accounts for TAF production, such that

$$P_{f}(x,t) = \sum_{i=1}^{N_{HYC}} P_{f,i}(x,t).$$
 (4)

In Eq. (4), N_{HYC} is the total number of hypoxic cells, and the function $P_{f,i}$ accounts for the TAF production of each hypoxic cell. We assume that the hypoxic cells are circles that do not move. We denote the center of the hypoxic cell i as $x_{HYC,i}$. Following [13], we can express $P_{f,i}$ as:

$$P_{f,i}(\boldsymbol{x},t) = \begin{cases} \mathcal{P}_f e^{-0.5t_i*}, & \text{if } |\boldsymbol{x} - \boldsymbol{x}_{\text{HYC},i}| < R_{\text{HYC}}, \\ 0, & \text{if } |\boldsymbol{x} - \boldsymbol{x}_{\text{HYC},i}| \ge R_{\text{HYC}}, \end{cases}$$
(5)

where R_{HYC} is the hypoxic cell radius and \mathcal{P}_f is the production rate. When a capillary approaches a hypoxic cell, the hypoxic cell receives the necessary nutrients and oxygen and, hence, TAF production stops. We model this process through the TAF-production decay time t_i^* , which we define

$$t_i * = \begin{cases} 0, & \text{if } t < T_i^*, \\ t - T_i *, & \text{if } t \ge T_i *, \end{cases}$$
 (6)

where T_i^* is the time at which the center of any TEC gets closer than d_{ox} to the center of the hypoxic cell i. The constant d_{ox} represents the characteristic oxygen diffusion length. The last term in the right-hand side of Eq. (3) accounts for the TAF natural degradation and the TAF uptake by the endothelial cells. The function U is defined as

$$U(c) = \begin{cases} U_u c, & \text{if } c \ge 0, \\ -U_d c, & \text{if } c < 0, \end{cases}$$
 (7)

where U_u is the endothelial cell uptake rate and U_d is the TAF decay rate.

We consider the following boundary conditions for the angiogenesis model:

$$0 = M\nabla(\mu(c) - \lambda^2 \Delta c) \cdot \mathbf{n}_{\partial O} \quad \text{on } \partial \Omega, \tag{8}$$

$$0 = M\lambda^2 \Delta c \qquad \text{on } \partial \Omega, \tag{9}$$

$$0 = D_0 \nabla f \cdot \mathbf{n}_{\partial \Omega} \qquad \text{on } \partial \Omega, \tag{10}$$

where $\partial \Omega$ is the boundary of Ω and $\mathbf{n}_{\partial \Omega}$ is the unit outward normal to $\partial \Omega$. These boundary conditions account for free flux of the vascular network [21, 22] and a permeable boundary to TAF advection, but not to TAF diffusion.

Discrete compartment

The discrete agents of the angiogenesis model represent TECs. We assume TECs are circles centered at x_{TEC} with radius R_{TEC} . A new TEC emerges centered at any point $x \in \Omega$ if the following conditions are achieved:

- $1. \quad c(\mathbf{x}) > c_{act},$
- 2. $f(x) > f_{act}$, 3. $d_{TEC}(x) > d_{Notch}$,

where c_{act} is the minimum value of c for TEC activation, f_{act} is the minimum TAF concentration for TEC activation, $d_{\text{TEC}}(x)$ is the distance from x to the center of the closest TEC, and d_{Notch} is the Delta-Notch distance [23]. Condition 1 ensures that TECs are created inside capillaries, condition 2 ensures that vascular growth is triggered above a minimum TAF concentration, and condition 3 accounts for the lateral inhibition mechanism [23]. TECs are deactivated when condition 2 is no longer achieved at x_{TEC} . TEC motion is directed by the TAF gradient according to the expression

$$\boldsymbol{u}_{\text{TEC}} = \begin{cases} \eta \nabla f, & \text{if } |\nabla f| < G_M, \\ \eta G_M \frac{\nabla f}{|\nabla f|}, & \text{if } |\nabla f| \ge G_M, \end{cases}$$
(11)

where u_{TEC} is the velocity of the TEC, the constant η is proportional to the chemotactic speed, and G_M is the cut-off value of $|\nabla f|$ for maximum TEC velocity.

TECs develop filopodia to detect neighboring capillaries and modify the direction of motion to conduct anastomosis [13]. We model filopodia by defining an array of checkpoints in an annular disk sector centered at x_{TEC} , with an angle of $\frac{2\pi}{3}$ centered around the direction of $\boldsymbol{u}_{\text{TEC}}$. The annular disk sector has an inner and outer radius of $2R_{\rm TEC}$ and $4R_{\rm TEC}$, respectively. At these checkpoints, we determine the existence of a capillary with the condition $c > c_{act}$. If the capillary exists, the direction of \boldsymbol{u}_{TEC} changes toward the successful checkpoint. To detect anastomosis, we perform a similar check with a circular disk of radius $1.5R_{\rm TEC}$. If $c > c_{act}$ at any checkpoint, we assume anastomosis has occurred and the TEC is deactivated.

The coupling between the continuous and discrete compartments is performed by imposing c = 1 in the region occupied by each TEC. More details about the model and the coupling between the continuous and discrete compartments may be found in [24, 25].



2.1.1 Weak form of the angiogenesis model

We obtain the weak form of the angiogenesis model by multiplying Eqs. (1) and (3) with weighting functions q_c and q_f , respectively, and integrating in Ω . We then integrate by parts and impose the boundary conditions defined in Eqs. (8)–(10). We define the forms

$$\begin{split} R_c(q_c,c,f) &= \int_{\Omega} q_c \frac{\partial c}{\partial t} \, \mathrm{d}V + \int_{\Omega} M \nabla q_c \cdot \nabla \mu(c) \, \mathrm{d}V \\ &+ \int_{\Omega} \Delta q_c M \lambda^2 \Delta c \, \mathrm{d}V \\ &- \int_{\Omega} q_c B(f) c H(c) \, \mathrm{d}V, \end{split} \tag{12}$$

$$\begin{split} R_f(q_f,c,f,\boldsymbol{u}) &= \int_{\varOmega} q_f \frac{\partial f}{\partial t} \, \mathrm{d}V \\ &+ \int_{\varOmega} q_f \nabla \cdot (\boldsymbol{u}f) \, \mathrm{d}V \\ &+ \int_{\varOmega} D_0 \nabla q_f \cdot \nabla f \, \mathrm{d}V \\ &- \int_{\varOmega} q_f P_f(f_{\mathrm{HYC}} - f) \, \mathrm{d}V \\ &+ \int_{\varOmega} q_f U(c) f \, \mathrm{d}V. \end{split} \tag{13}$$

We next define the Sobolev and Lebesgue spaces:

Definition 1 $L^p(\Omega)$ is a Lebesgue space defined as

$$L^{p}(\Omega) = \{ \Psi : \Omega \to \mathbb{R} \} \text{ such that } \|\Psi\|_{L^{p}(\Omega)}^{p} = \int_{\Omega} |\Psi|^{p} \, \mathrm{d}V < \infty,$$
(14)

where p is a natural number, $\|\cdot\|$ is the norm, and $\|\cdot\|$ is the absolute value.

 $H^{\ell}(\Omega)$ is the Sobolev space associated with the L^2 norm and is defined as

$$H^{\ell}(\Omega) = \left\{ \Psi \in L^{2}(\Omega) : D^{\beta}\Psi \in L^{2}(\Omega) \ \forall \ |\beta| \le \ell \right\}, \tag{15}$$

where β is a multi-index, $D^{\beta}\Psi$ is the mixed partial, weak derivative of Ψ [26], and ℓ is a natural number.

The angiogenesis problem can be stated as

Definition 2 Find $(c,f) \in H^2(\Omega) \times H^1(\Omega)$ such that for all $(q_c,q_f) \in H^2(\Omega) \times H^1(\Omega)$

$$R_c(q_c, c, f) + R_f(q_f, c, f, \mathbf{u}) = 0.$$
 (16)

2.2 Coupled Stokes-Darcy flow

In this section, we first describe the coupled Stokes–Darcy equations for incompressible fluid flow. The model is comprised of the Stokes equations posed in $\Omega_S(t)$, the Darcy equations posed in $\Omega_D(t)$, and the interface conditions posed on $\Gamma(t)$, where $\Gamma(t)$ is the interface that separates Ω_S and Ω_D (see Fig. 1). Next, we derive the weak form of the Stokes–Darcy problem, where the integrals are posed in $\Omega_S(t)$, $\Omega_D(t)$, and $\Gamma(t)$. We denote this description of the weak form as the sharp-interface weak form of the problem.

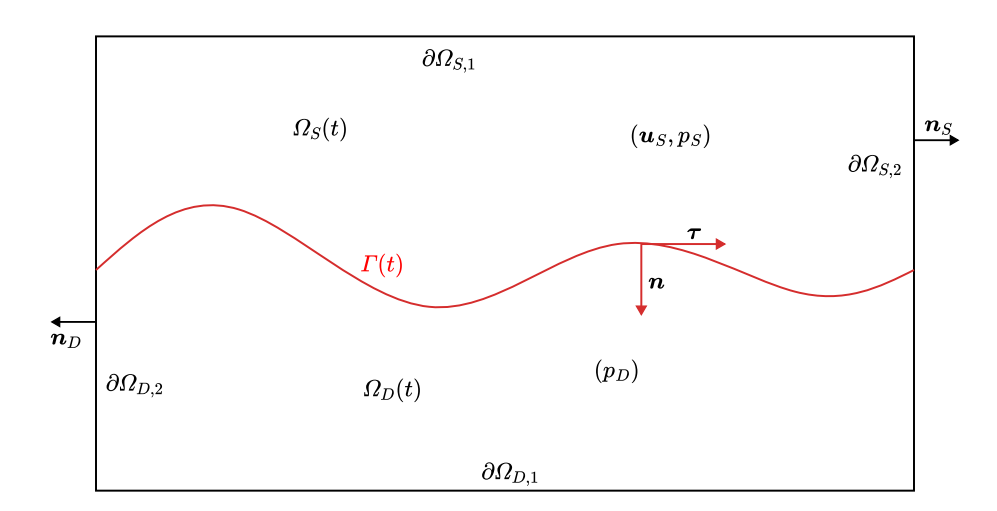


Fig. 1 Sketch of the computational domain Ω . The Stokes and Darcy domains are represented by $\Omega_S(t)$ and $\Omega_D(t)$, respectively. The boundary of Ω may be divided into four regions, namely, $\partial\Omega_{S,1}$, $\partial\Omega_{S,2}$, $\partial\Omega_{D,1}$, and $\partial\Omega_{D,2}$, where the indices S and D refer to the Stokes and Darcy domains, respectively, and the indices 1 and 2 refer to Dirichlet and Neumann boundary conditions, respectively. The unit outward

normal to Ω in Ω_S and Ω_D are denoted as \mathbf{n}_S and \mathbf{n}_D , respectively. Ω_S and Ω_D are separated by the moving interface $\Gamma(t)$. The unit normal to Γ pointing into Ω_D is denoted as \mathbf{n} and the unit tangent vector is denoted as $\boldsymbol{\tau}$. In the sharp-interface description, we solve for the Stokes velocity (\mathbf{u}_S) and pressure (p_S) in Ω_S and the Darcy pressure (p_D) in Ω_D



Finally, we leverage the phase-field method and derive the diffuse-interface approximation of the weak form of the Stokes–Darcy problem, where the integrals are posed in Ω .

2.2.1 Sharp-interface description of the Stokes–Darcy problem

Stokes flow

The Stokes equations for incompressible fluid flow read

$$\nabla \cdot \boldsymbol{u}_{S} = 0 \quad \text{in } \Omega_{S}, \tag{17}$$

$$-\nabla \cdot \boldsymbol{\sigma} = \boldsymbol{b} \quad \text{in } \Omega_{S}, \tag{18}$$

where $\mathbf{u}_S(\mathbf{x}_S, t)$, with $\mathbf{x}_S \in \Omega_S$, is the fluid velocity in Ω_S and \mathbf{b} is the body force per unit mass. The stress tensor is defined as $\sigma = -p_S \mathbb{I} + 2\nu \nabla^S \mathbf{u}_S$, where $p_S(\mathbf{x}_S, t)$ is the pressure normalized by the fluid density, \mathbb{I} is the identity tensor, ν is the kinematic viscosity, and ∇^S is the symmetric gradient defined as $\nabla^S = \frac{1}{2}(\nabla + \nabla^T)$.

We consider the following boundary conditions on $\partial \Omega_{S,1}$ and $\partial \Omega_{S,2}$ (see Fig. 1):

$$\mathbf{u}_{S} = \bar{\mathbf{u}}_{S} \text{ on } \partial\Omega_{S,1}, \qquad \sigma \mathbf{n}_{S} = \bar{\mathbf{t}} \text{ on } \partial\Omega_{S,2},$$
 (19)

where \bar{u}_S is the boundary fluid velocity, \bar{t} is the boundary traction, and n_S is the outward normal to $\partial \Omega$ in Ω_S (Fig. 1).

Darcy flow

The equations for incompressible fluid flow through a saturated porous medium (i.e., the interstitium) are expressed as

$$\nabla \cdot \boldsymbol{u}_D = 0 \quad \text{in } \Omega_D, \tag{20}$$

$$\boldsymbol{u}_D = -\frac{k}{\mu} \nabla p_D \quad \text{in } \Omega_D, \tag{21}$$

where $u_D(x_D, t)$ is the Darcy velocity, k is the interstitium permeability, μ is the dynamic viscosity of the interstitial fluid, and $p_D(x_D, t)$ is the interstitial fluid pressure, with $x_D \in \Omega_D$. We can reduce the number of unknowns by substituting Eq. (21) into Eq. (20). The final equation reads

$$-\nabla \cdot \left(\frac{k}{\mu} \nabla p_D\right) = 0 \quad \text{in } \Omega_D. \tag{22}$$

We consider the following boundary conditions on $\partial \Omega_{D,1}$ and $\partial \Omega_{D,2}$ (see Fig. 1):

$$p_D = \bar{p}_D \text{ on } \partial \Omega_{D,1}, \qquad \boldsymbol{u}_D \cdot \boldsymbol{n}_D = \bar{u}_D \text{ on } \partial \Omega_{D,2},$$
 (23)

where \bar{p}_D is the boundary Darcy pressure, \bar{u}_D is the boundary Darcy velocity in the normal direction, and \mathbf{n}_D is the unit outward normal to $\partial \Omega$ in Ω_D (Fig. 1).

Stokes-Darcy interface conditions

The Stokes and Darcy equations are coupled through the interface conditions imposed on $\Gamma(t)$. We denote the unit normal vector to Γ pointing into Ω_D as n, and the unit tangent vector to Γ as τ (Fig. 1). The interface conditions are expressed as

$$\mathbf{u}_S \cdot \mathbf{n} = \mathbf{u}_D \cdot \mathbf{n} \quad \text{on } \Gamma,$$
 (24)

$$\boldsymbol{n} \cdot \boldsymbol{\sigma} \boldsymbol{n} = -\frac{p_D}{\rho} \quad \text{on } \Gamma, \tag{25}$$

$$\alpha \frac{v}{\sqrt{k}} (\boldsymbol{u}_{S} - \boldsymbol{u}_{D}) \cdot \boldsymbol{\tau} = -\boldsymbol{\tau} \cdot \boldsymbol{\sigma} \boldsymbol{n} \quad \text{on } \Gamma,$$
(26)

where α is the Beavers-Joseph parameter. We assume that these fluid properties take a constant value. Note that we include the density into Eq. (25), because the stress tensor σ (and, hence, p_s) is normalized by the fluid density ρ , but not the Darcy pressure p_D . Equation (24) ensures mass conservation across the interface, Eq. (25) enforces the balance of normal traction across the interface, and Eq. (26) is an empirical law proposed by Beavers and Joseph [27] that relates the Stokes shear stress with the difference between the Stokes and Darcy tangential velocities. The Darcy tangential velocity is usually smaller than the Stokes tangential velocity on Γ , which allows us to assume $(u_S - u_D) \cdot \tau \approx u_S \cdot \tau$ in Eq. (26). This modification is called Beavers-Joseph-Saffman law and is widely used in the literature [27–29]. The friction parameter α controls the transvascular permeability [30] and is experimentally estimated. Due to the lack of experiments to estimate α for vascular flows, we adjust α , such that it matches experimentally observed values of transvascular permeability.

2.2.2 Sharp-interface weak form of the Stokes–Darcy problem

We obtain the sharp-interface weak form of the Stokes–Darcy problem by multiplying Eqs. (17), (18), and (22) with weighting functions and integrating in the corresponding domains. We next integrate by parts and substitute the natural boundary conditions defined in Eqs. (19) and (23). The sharp-interface description of the Stokes–Darcy problem can be stated as

Definition 3 Find $(\boldsymbol{u}_S, p_S, p_D) \in H^1(\Omega_S) \times L^2(\Omega_S) \times H^1(\Omega_D)$ such that for all $(\boldsymbol{w}, q_S, q_D) \in H^1(\Omega_S) \times L^2(\Omega_S) \times H^1(\Omega_D)$



$$0 = \int_{\Omega_{S}} 2\nu \nabla \mathbf{w} : \nabla^{S} \mathbf{u}_{S} \, dV - \int_{\Omega_{S}} (\nabla \cdot \mathbf{w}) p_{S} \, dV$$

$$- \int_{\Omega_{S}} \mathbf{w} \cdot \mathbf{b} \, dV$$

$$- \int_{\partial \Omega_{S,2}} \mathbf{w} \cdot \mathbf{\bar{t}} \, dS - \int_{\Gamma} \mathbf{w} \cdot \boldsymbol{\sigma} \mathbf{n} \, dS$$

$$+ \int_{\Omega_{S}} q_{S} (\nabla \cdot \mathbf{u}_{S}) \, dV$$

$$+ \int_{\Omega_{D}} \frac{k}{\mu} \nabla q_{D} \cdot \nabla p_{D} \, dV + \int_{\partial \Omega_{D,2}} q_{D} \bar{\mathbf{u}}_{D} \, dS$$

$$- \int_{\Gamma} q_{D} \mathbf{u}_{D} \cdot \mathbf{n} \, dS.$$

$$(27)$$

We incorporate the interface conditions into the weak form by using Eqs. (24)–(26) to replace the boundary integrals over Γ in Eq. (27) in the following manner:

$$-\int_{\Gamma} \mathbf{w} \cdot \boldsymbol{\sigma} \mathbf{n} \, dS = \int_{\Gamma} \frac{p_D}{\rho} \mathbf{w} \cdot \mathbf{n} \, dS + \int_{\Gamma} \alpha \frac{\nu}{\sqrt{k}} (\mathbf{u}_S \cdot \boldsymbol{\tau}) (\mathbf{w} \cdot \boldsymbol{\tau}) \, dS,$$
 (28)

$$-\int_{\Gamma} q_D \boldsymbol{u}_D \cdot \boldsymbol{n} \, \mathrm{d}S = -\int_{\Gamma} q_D \boldsymbol{u}_S \cdot \boldsymbol{n} \, \mathrm{d}S. \tag{29}$$

2.2.3 Diffuse-interface approximation

The weak form defined in Eq. (27) involves integrals in moving domains. The numerical solution of Eq. (27) requires the use of moving meshes and entails important numerical challenges. Here, we leverage the phase-field method and reformulate the Stokes–Darcy problem by deriving a diffuse-interface approximation of the weak form that involves integrals in Ω only. Thus, we can solve the diffuse-interface weak form by using a single and fixed mesh. We start by defining the phase-field variables and properties that we need to derive the diffuse-interface weak form.

We use the phase-field variable $\phi(x,t)$, with $x \in \Omega$, to capture the domain $\Omega_S(t)$, such that $\phi=1$ in Ω_S , $\phi=0$ in Ω_D , and ϕ smoothly transitions from 0 to 1 across the interface Γ (see Fig. 2). We define the phase field ϕ as a function of the vascular density c (see Sect. 2.1), which is also a phase-field variable. Note that c ranges from c=-1 in the interstitium (Ω_D) to c=1 inside the capillaries (Ω_S) . Thus, we define ϕ as

$$\phi = \frac{1+c}{2}.\tag{30}$$

Likewise, we capture the domain $\Omega_D(t)$ with the expression $(1 - \phi)$.

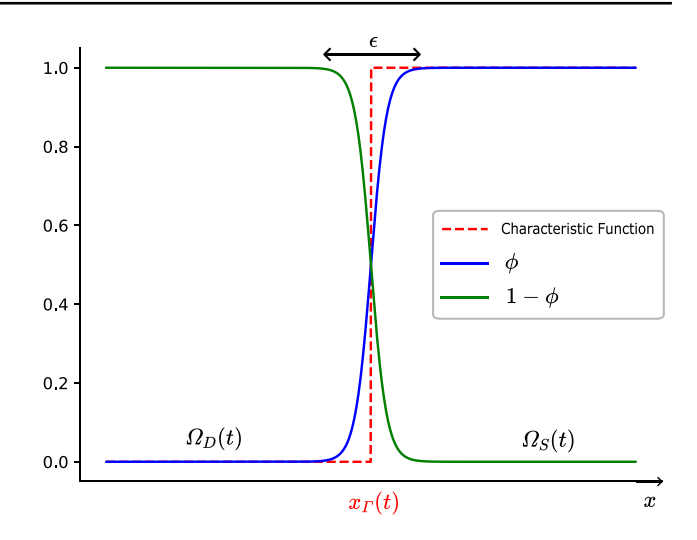


Fig. 2 1D representation of the phase field ϕ that captures the Stokes domain $\Omega_S(t)$. The phase field ϕ is an approximation of the characteristic function (marked by the dashed red line) centered at the interface $x_\Gamma(t)$. The characteristic function is a discontinuous function that takes the value of 0 in the Darcy domain and 1 in the Stokes domain. The parameter ϵ represents the characteristic width of the interface. The figure also shows the complementary phase field $1-\phi$ that captures the Darcy domain $\Omega_D(t)$ (color figure online)

To discuss the phase-field properties, we first define weighted function spaces following [31]:

Definition 4 For a positive weight function ω , a positive integer r, and a bounded domain Ω , we define weighted Lebesgue spaces and their norms as

$$L^{r}(\Omega, \omega) = \left\{ \Psi : \Omega \to \mathbb{R} : |\Psi|^{r} \omega \in L^{1}(\Omega) \right\},$$

$$\|\Psi\|_{L^{r}(\Omega, \omega)}^{r} = \int_{\Omega} |\Psi|^{r} \omega \, dV.$$
(31)

We define the weighted Sobolev space associated with the L^2 norm as

$$H^{\ell}(\Omega,\omega) = \left\{ \Psi \in L^{2}(\Omega,\omega) : D^{\beta}\Psi \in L^{2}(\Omega,\omega) \ \forall \ |\beta| \le \ell \right\}. \tag{32}$$

Let us consider a function $g(x, t) \in L^2(\Omega, \phi)$. The first phase-field property [18, 32] can be stated as

$$\int_{\Omega} \phi(\mathbf{x}, t) g(\mathbf{x}, t) \, \mathrm{d}V \to \int_{\Omega_{\epsilon}} g(\mathbf{x}, t) \, \mathrm{d}V \quad \text{as } \epsilon \to 0, \tag{33}$$

where ϵ is the parameter that controls the width of the diffuse interface (see Fig. 2). The phase-field formulation has an analogous property for integrals on interfaces, which reads

$$\int_{\Omega} \delta_{\Gamma}(\phi) g(\mathbf{x}, t) \, dV \to \int_{\Gamma} g(\mathbf{x}, t) \, dS \quad \text{as } \epsilon \to 0,$$
 (34)



where the function $\delta_{\Gamma}(\phi)$ is a marker of the interface Γ , such that δ_{Γ} is zero far from the interface and takes a positive value around the interface. The marker $\delta_{\Gamma}(\phi)$ may take different expressions (see [18] for more details). Here, we take $\delta_{\Gamma}(\phi) = |\nabla \phi|$.

Based on the properties defined in Eqs. (33) and (34), we can approximate the integrals of g(x, t) as

$$\int_{\Omega_{S}} g(\mathbf{x}, t) \, dV \approx \int_{\Omega} \phi g(\mathbf{x}, t) \, dV,$$

$$\int_{\Omega_{D}} g(\mathbf{x}, t) \, dV \approx \int_{\Omega} (1 - \phi) g(\mathbf{x}, t) \, dV,$$
(35)

$$\int_{\Gamma} g(\mathbf{x}, t) \, \mathrm{d}S \approx \int_{\Omega} g(\mathbf{x}, t) |\nabla \phi| \, \mathrm{d}V, \tag{36}$$

$$\int_{\partial\Omega_{S,2}} g(\mathbf{x}, t) \, \mathrm{d}S \approx \int_{\partial\Omega_{S,2}^e} \phi \, g(\mathbf{x}, t) \, \mathrm{d}S,$$

$$\int_{\partial\Omega_{D,2}} g(\mathbf{x}, t) \, \mathrm{d}S \approx \int_{\partial\Omega_{D,2}^e} (1 - \phi) \, g(\mathbf{x}, t) \, \mathrm{d}S,$$
(37)

where the Neumann boundary extension $\partial\Omega^e_{S,2}$ (respectively, $\partial\Omega^e_{D,2}$) represents an extension of $\partial\Omega_{S,2}$ (respectively, $\partial\Omega_{D,2}$) off Γ along the corresponding edge of Ω . We localize the integral to $\partial\Omega_{S,2}$ (respectively, $\partial\Omega_{D,2}$) by including the phase field ϕ (respectively, $1-\phi$) in the boundary integral in Eq. (37). Analogously, we define the Dirichlet boundary extension $\partial\Omega^e_{S,1}$ (respectively, $\partial\Omega^e_{D,1}$) as an extension of $\partial\Omega_{S,2}$ (respectively, $\partial\Omega_{D,2}$) off Γ along the corresponding edge of Ω . Finally, we can define the normal to Γ as a function of ϕ , such that $n=-\nabla\phi/|\nabla\phi|$. We construct the tangent vector τ by rotating n by 90° in the counter-clockwise direction.

2.2.4 Diffuse-interface weak form of the Stokes–Darcy problem

Using Eqs. (35)–(37), we aim to approximate integrals in the sharp-interface weak form (Eq. (27)). In Eqs. (35)–(37), the support of $g(\mathbf{x},t)$ is Ω . However, the support of the Stokes–Darcy unknowns \mathbf{u}_S , p_S , and p_D is Ω_S , Ω_S , and Ω_D , respectively. To utilize Eqs. (35)–(37) to approximate the sharp-interface weak form, we need to consider the unknowns whose support is Ω . Thus, we define the diffuse-interface unknowns $\mathbf{u}_S^\epsilon(\mathbf{x},t)$, $p_S^\epsilon(\mathbf{x},t)$, and $p_D^\epsilon(\mathbf{x},t)$ whose support is Ω . The diffuse interface unknowns $\mathbf{u}_S^\epsilon(\mathbf{x},t)$ and $p_S^\epsilon(\mathbf{x},t)$ (respectively, $p_D^\epsilon(\mathbf{x},t)$) approximate \mathbf{u}_S and p_S (respectively, $p_D^\epsilon(\mathbf{x},t)$) in Ω_S (respectively, Ω_D). The values of the diffuse-interface unknowns $\mathbf{u}_S^\epsilon(\mathbf{x},t)$ and $p_S^\epsilon(\mathbf{x},t)$ (respectively, $p_D^\epsilon(\mathbf{x},t)$) far from Γ in Ω_D (respectively, Ω_D) are not relevant. Further, there are several known quantities in Eq. (27) (such as \mathbf{b}) that are not completely supported in Ω . We define the

diffuse-interface extensions ${m b}^e, {ar t}^e, {ar u}_D^e, {ar u}_S^e$ and ${ar p}_D^e$ whose support is in Ω and result from extending ${m b}, {ar t}, {ar u}_D, {ar u}_S$ and ${ar p}_D$ respectively off Γ constant in the normal direction.

Next, we define the following forms where we approximate the integrals in the sharp-interface weak form (Eq. (27)) using the properties defined in Sect. 2.2.3:

$$R_{u_{S}}(\boldsymbol{w}, \boldsymbol{u}_{S}^{\epsilon}, p_{S}^{\epsilon}, p_{D}^{\epsilon}, \boldsymbol{\phi}) = \int_{\Omega} 2\nu \boldsymbol{\phi} \nabla \boldsymbol{w} : \nabla^{S} \boldsymbol{u}_{S}^{\epsilon} \, dV$$

$$- \int_{\Omega} \boldsymbol{\phi} (\nabla \cdot \boldsymbol{w}) p_{S}^{\epsilon} \, dV - \int_{\Omega} \boldsymbol{\phi} \boldsymbol{w} \cdot \boldsymbol{b}^{\epsilon} \, dV$$

$$- \int_{\partial \Omega_{S,2}^{\epsilon}} \boldsymbol{\phi} \, \boldsymbol{w} \cdot \overline{\boldsymbol{t}}^{\epsilon} \, dS$$

$$+ \int_{\Omega} \frac{p_{D}^{\epsilon}}{\rho} \boldsymbol{w} \cdot \boldsymbol{n} \, |\nabla \boldsymbol{\phi}| \, dV$$

$$+ \int_{\Omega} \alpha \frac{\nu}{\sqrt{k}} (\boldsymbol{u}_{S}^{\epsilon} \cdot \boldsymbol{\tau}) (\boldsymbol{w} \cdot \boldsymbol{\tau}) \, |\nabla \boldsymbol{\phi}| \, dV,$$

$$(38)$$

$$R_{p_S}(q_S, \boldsymbol{u}_S^{\epsilon}, \boldsymbol{\phi}) = \int_{\Omega} \boldsymbol{\phi} q_S(\nabla \cdot \boldsymbol{u}_S^{\epsilon}) \, \mathrm{d}V, \tag{39}$$

$$R_{p_{D}}(q_{D}, \boldsymbol{u}_{S}^{\epsilon}, p_{D}^{\epsilon}, \boldsymbol{\phi}) = \int_{\Omega} (1 - \boldsymbol{\phi}) \frac{k}{\mu} \nabla q_{D} \cdot \nabla p_{D}^{\epsilon} \, dV$$

$$+ \int_{\partial \Omega_{D,2}^{\epsilon}} (1 - \boldsymbol{\phi}) \, q_{D} \bar{\boldsymbol{u}}_{D}^{\epsilon} \, dS \qquad (40)$$

$$- \int_{\Omega} q_{D} \boldsymbol{u}_{S}^{\epsilon} \cdot \boldsymbol{n} |\nabla \boldsymbol{\phi}| \, dV.$$

Here, we assume the fluid properties (v, ρ, k, μ) take constant values. Otherwise, we should consider the extended functions of these properties off Γ constant in the normal direction.

Finally, the diffuse-interface approximation of the Stokes-Darcy problem can be stated as

Definition 5 Find $(\boldsymbol{u}_{S}^{\epsilon}, p_{S}^{\epsilon}, p_{D}^{\epsilon}) \in H^{1}(\Omega, \phi) \times L^{2}(\Omega, \phi) \times H^{1}(\Omega, 1 - \phi)$ such that for all $(\boldsymbol{w}, q_{S}, q_{D}) \in H^{1}(\Omega, \phi) \times L^{2}(\Omega, \phi) \times H^{1}(\Omega, 1 - \phi)$

$$R_{u_S}(\mathbf{w}, \mathbf{u}_S^{\epsilon}, p_S^{\epsilon}, p_D^{\epsilon}, \phi) + R_{p_S}(q_S, \mathbf{u}_S^{\epsilon}, \phi)$$

$$+ R_{p_D}(q_D, \mathbf{u}_S^{\epsilon}, p_D^{\epsilon}, \phi) = 0.$$

$$(41)$$

Further, the Dirichlet boundary conditions \bar{u}_S^e and \bar{p}_D^e are strongly imposed on $\partial \Omega_{S,1}^e$ and $\partial \Omega_{D,1}^e$, respectively.

Due to the non-zero value of ϵ , the diffuse-interface weak form (Definition 5) is not equivalent to the sharp-interface weak form (Definition 3). Hence, the diffuse-interface solution $\boldsymbol{u}_S^\epsilon$ and p_S^ϵ (respectively, p_D^ϵ) will only be approximately equal to \boldsymbol{u}_S and p_S (respectively, p_D) in Ω_S (respectively, Ω_D). We call the discrepancy between the diffuse and sharp-interface solutions the modeling error. The modeling error



converges to zero when we refine ϵ . More details on the convergence rates of this error may be found in [31].

The coupling between the angiogenesis and the Stokes-Darcy flow model is completed with the definition of the *multiphysics* velocity u(x, t), with $x \in \Omega$, defined as

$$\boldsymbol{u} = \phi \boldsymbol{u}_{S}^{\epsilon} + (1 - \phi) \boldsymbol{u}_{D}^{\epsilon},\tag{42}$$

where ϕ is computed with Eq. (30) and u_D^ϵ is computed with Eq. (21) considering p_D^ϵ instead of p_D . The flow velocity u affects the transport of TAF in the angiogenesis model. For visualization purposes, we also define the *multiphysics* pressure p(x,t) as $p = \phi \rho p_S^\epsilon + (1-\phi) p_D^\epsilon$.

3 Numerical method

3.1 Implementation details

The phase field c may display values slightly lower than -1 and larger than 1 due to numerical errors and the proliferation term (see Eq. (1)). To limit the values of $\phi(x, t)$ between 0 and 1, instead of using Eq. (30), we redefine $\phi(c)$ as

$$\phi^*(c) = \frac{c - \max(c)}{\max(c) - \min(c)},\tag{43}$$

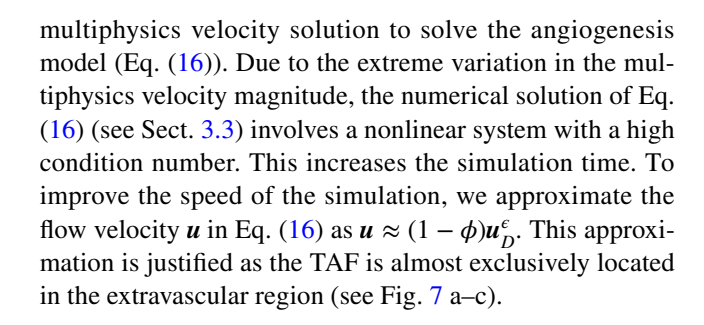
where $\min(c)$ and $\max(c)$ are the minimum and maximum values of c(x,t) in Ω . Equation (43) ensures that $\phi^*(x,t) \in [0,1]$ while keeping the characteristic tanh-profile across the interface.

The diffuse-interface weak form of the Stokes–Darcy problem (Definition 5) includes integrals that are zero over large regions in Ω (e.g., the Jacobian of the residual R_{u_S} equals zero far from Ω_S , because $\phi=0$ far from Ω_S). Due to this effect, the numerical solution of Eq. (41) (see Sect. 3.3) involves a linear system that is ill-conditioned. There are different approaches to fix this issue. Here, we resort to a regularization of the phase field ϕ , such that ϕ and $(1-\phi)$ never take the value 0, but values close to 0 that do not affect the problem dynamics [31]. We define the regularized phase field ϕ_F as

$$\phi_{\kappa}(c) = (1 - 2\kappa)\phi^{*}(c) + \kappa, \tag{44}$$

where $\phi^*(c)$ is defined in Eq. (43) and $\kappa = 10^{-4}$ is the regularization parameter. We replace $\phi(x,t)$ by $\phi_{\kappa}(x,t)$ in the diffuse-interface weak form of the Stokes–Darcy problem (Eq. (41)). This procedure leads to linear systems with lower condition numbers, while the dynamics of the Stokes–Darcy problem are not affected.

The multiphysics velocity u represents the velocity of the fluid in both intravascular and extravascular regions. The intravascular flow velocity magnitude is significantly higher than the extravascular flow magnitude. We use the



3.2 Stabilized weak form of the Stokes–Darcy problem

The diffuse-interface weak form of the Stokes–Darcy problem (Definition 5) constitutes a saddle point problem. Thus, we require the discrete spaces to satisfy the Ladyzhens-kaya–Babuška–Brezzi (LBB) condition [33]. Due to the inherent complexity of the diffuse-interface approximation of the Stokes–Darcy problem, it is unclear which are the discrete spaces that satisfy the LBB condition. To circumvent this requirement, we incorporate stabilization terms into the diffuse-interface weak form, based on the Galerkin Least Squares (GLS) formulation [33]. We define the stabilized diffuse-interface weak form of the Stokes–Darcy problem as

$$R_{SD}(\boldsymbol{w}, q_{S}, q_{D}, \boldsymbol{u}_{S}^{\epsilon}, p_{S}^{\epsilon}, p_{D}^{\epsilon}, c)$$

$$= R_{u_{S}}(\boldsymbol{w}, \boldsymbol{u}_{S}^{\epsilon}, p_{S}^{\epsilon}, p_{D}^{\epsilon}, \phi_{\kappa}(c))$$

$$+ R_{p_{S}}(q_{S}, \boldsymbol{u}_{S}^{\epsilon}, \phi_{\kappa}(c))$$

$$+ R_{p_{D}}(q_{D}, \boldsymbol{u}_{S}^{\epsilon}, p_{D}^{\epsilon}, \phi_{\kappa}(c))$$

$$+ \sum_{e=1}^{N_{e}} \int_{\Omega_{e}} \tau_{GLS}(\nabla p_{S}^{\epsilon} - 2\nu \nabla \cdot (\nabla^{S} \boldsymbol{u}_{S}^{\epsilon}) - \boldsymbol{b}^{\epsilon})(\nabla q_{S}$$

$$- 2\nu \nabla \cdot (\nabla^{S} \boldsymbol{w}))\phi_{\kappa}(c) \, dV,$$

$$(45)$$

where $\phi_{\kappa}(c)$ is defined in Eq. (44), N_e is the number of elements of the mesh, Ω_e denotes the space occupied by element e, and τ_{GLS} is the stabilization parameter [34] defined as

$$\tau_{GLS} = \frac{h_{m,e}^2}{4\nu},\tag{46}$$

where $h_{m,e}$ is the size of the mesh element e. Since we use a triangular mesh for the Stokes-Darcy equations, $h_{m,e}$ is defined as the radius of the circumcircle of element e.

3.3 Spatial and time discretization

We use Finite-Element Analysis to solve our flow-mediated angiogenesis model. We implement a staggered algorithm to solve the coupled problem. At each time step, we first solve the angiogenesis problem considering a fixed velocity u, and then, we use the updated vascular geometry to compute ϕ_{κ}



and solve the Stokes-Darcy problem. In the following paragraphs, we provide more details about the staggered algorithm and the spatial and time discretization.

3.3.1 Spatial discretization

We use two different spatial discretizations to solve the Stokes–Darcy problem and the angiogenesis problem.

The spatial discretization of the Stokes–Darcy problem (Definition 5) requires discrete solution and weighting function spaces that are a subset of $H^1(\Omega, \phi_\kappa)$. We denote the discrete solution $(\boldsymbol{u}_S^{\epsilon,h}, p_S^{\epsilon,h}, p_D^{\epsilon,h}) \in \mathcal{W}^h$ and the discrete weighting functions $(\boldsymbol{w}^h, q_S^h, q_D^h) \in \mathcal{W}^h$, where \mathcal{W}^h is a discrete space composed of first-order Lagrange basis functions. The discrete diffuse-interface weak form of the Stokes–Darcy problem is obtained by replacing the unknowns and weighting functions by their discrete approximations in Eq. (45).

The spatial discretization of the angiogenesis problem (Definition 2) is more restrictive, since it requires discrete solution and weighting function spaces that are a subset of $H^2(\Omega)$. We solve the angiogenesis problem using Isogeometric Analysis [35, 36], which is a generalization of the Finite-Element Method that uses splines as basis functions. We denote the discrete solution $(c^h, f^h) \in \mathcal{V}^h$ and the discrete weighting functions $(q_c^h, q_f^h) \in \mathcal{V}^h$, where \mathcal{V}^h is a discrete space comprised of quadratic \mathcal{C}^1 -continuous B-splines. The discrete weak form of the angiogenesis problem is obtained by replacing c, f, q_c , and q_f by their discrete approximations in Eq. (16).

Here, we use a uniform mesh composed of square elements to construct V^h , while we use a mesh composed of triangular elements to construct W^h . In general, the triangle mesh used in the Stokes-Darcy problem is coarser than the square mesh used in the angiogenesis problem. Thus, we exploit the capability of controlling the resolution of both meshes independently to speed up the simulations.

To solve Eq. (16), we need the value of the multiphysics velocity \boldsymbol{u} at the Gaussian quadrature points of the elements that comprise the quadratic B-spline mesh. We interpolate these values using the solution vector of Eq. (45), which is constructed using Lagrange basis functions of the triangular mesh. We use a similar method to transfer the phase field c from the quadratic B-spline mesh to the triangular mesh to solve the Stokes–Darcy problem (Definition 5).

3.3.2 Time discretization

We divide the time interval of interest [0, T] into N_T time steps (t_n, t_{n+1}) , where T is the final time of the simulation. We denote the discrete solution of the Stokes–Darcy problem and the angiogenesis problem at time t_n as $(\boldsymbol{u}_n^n, p_n^n, p_n^n)$ and

 (c^n, f^n) , respectively, where we removed the superscripts h and ε for the sake of simplicity. Assuming that we know the discrete solution at time t_n , namely $(\boldsymbol{u}_S^n, p_S^n, p_D^n, c^n, f^n)$, we obtain the discrete solution at time t_{n+1} , namely $(\boldsymbol{u}_S^{n+1}, p_S^{n+1}, p_D^{n+1}, c^{n+1}, f^{n+1})$, in the following way:

First, we solve the angiogenesis problem (Definition 2) considering a fixed velocity $u = u^n$, which is calculated using ϕ_{κ}^n instead of ϕ . We use the generalized- α method [37, 38] to solve the angiogenesis problem (more details about the implementation in [13, 24]). We use the Newton–Raphson method to solve the nonlinear system of Eq. (16). Each iteration of the Newton–Raphson algorithm involves the solution of a linear system, which we carry out using the GMRES method [39].

Second, we use the solution of the angiogenesis problem (c^{n+1}, f^{n+1}) to compute ϕ_{κ}^{n+1} following Eqs. (43) and (44). We then take ϕ_{κ}^{n+1} and solve the Stokes–Darcy problem (see Eq. (45)) to obtain the Stokes–Darcy solution $(\boldsymbol{u}_{S}^{n+1}, p_{S}^{n+1}, p_{D}^{n+1})$. We use MUMPS [40] to solve the linear equations of the Stokes–Darcy problem.

To speed up the simulations, we implement an adaptive time stepping scheme, where the time step size $(t_{n+1} - t_n)$ depends on the number of Newton–Raphson iterations used to solve the angiogenesis problem (more details in [11]).

3.3.3 Computational Details

We use a combination of the FEniCS [41–46] computing platform and in-house research code to simulate the flow-mediated anagiogenesis model. Each simulation in sections 4.2 and 4.3 is performed using 64 cores. We ran the simulations using a triangular mesh (used to build \mathcal{W}^h) with 128,954 elements for the flow problem and a quadratic B-spline mesh (used to build \mathcal{V}^h) with 256 × 256 elements for the angiogenesis problem.

The parameter values used in the simulations are listed in Table 1. The values of M, λ , B_0 , f_p , D_0 , f_{HYC} , \mathcal{P}_f , U_u , U_d , d_{ox} , c_{act} , f_{act} , d_{Notch} and R_{TEC} presented in Table 1 are estimated in [13]. Following [15], we set the values for the chemotactic constant η and the cut-off velocity G_M , such that ηG_M equals the maximum TEC velocity of 0.35 μ m/s. The flow model parameters $(\rho, \nu, \mu \text{ and } k)$ have been obtained from [47].

4 Results

In this section, we demonstrate the capabilities of the flow-mediated angiogenesis model. We first validate the Stokes-Darcy flow model by comparing the numerical solution with an exact manufactured solution on a rectangular domain. Then, we present two numerical simulations of



Table 1 Parameter values

| | Description | Value | References |
|--------------------|---|--|------------|
| M | Mobility | $1.002 \times 10^{-11} \mathrm{cm}^2 \mathrm{s}^{-1}$ | [25] |
| λ | Interface width | $1.25~\mu\mathrm{m}$ | [48] |
| B_0 | Proliferation rate | $4.987 \times 10^{-6} \mathrm{ml}\mathrm{ng}^{-1}\mathrm{s}^{-1}$ | [15] |
| f_p | TAF concentration for highest proliferation | $54 \mathrm{ng}\mathrm{ml}^{-1}$ | [15] |
| D_0 | TAF diffusion coefficient | $1.002 \times 10^{-7} \mathrm{cm^2s^{-1}}$ | [49] |
| f_{HYC} | Maximum TAF value | 180ng ml^{-1} | [50, 51] |
| \mathcal{P}_f | TAF production rate | $6.410 \times 10^{-2} \mathrm{1s^{-1}}$ | Numerical |
| U_u | Endothelial cell uptake rate | $4.006 \times 10^{-1} \ 1 \ s^{-1}$ | Estimated |
| U_d | TAF natural decay | $6.410 \times 10^{-5} \mathrm{1s^{-1}}$ | [52] |
| d_{ox} | Nutrient and oxygen diffusion length | $25 \mu m$ | [53, 54] |
| c_{act} | TEC activation condition | 0.9 | [15] |
| f_{act} | TEC activation condition | 0.72 ng ml^{-1} | [25] |
| $d_{ m Notch}$ | Delta-Notch distance | $80 \mu \mathrm{m}$ | [53, 54] |
| R_{TEC} | TEC radius | 5 μm | [55] |
| $R_{ m HYC}$ | Hypoxic cell radius | $6.25 \mu\mathrm{m}$ | Estimated |
| η | Chemotactic constant | $0.243 \ \mu \text{m}^2 \ \text{ng}^{-1} \ \text{s}^{-1} \ \text{ml}^{-1}$ | [15] |
| G_M | Cutoff value for TEC velocity | 1.44 ng ml ⁻¹ μ m ⁻¹ | [15] |
| ν | Kinematic viscosity | $3.1 \times 10^{-6} \text{ m}^2 \text{ s}^{-1}$ | [47] |
| μ | Dynamic viscosity | $3.1 \times 10^{-3} \mathrm{kg} \;\mathrm{m}^{-1} \mathrm{s}^{-1}$ | [47] |
| k | Permeability | $1.55 \times 10^{-14} \mathrm{m}^2$ | [47] |
| ρ | Fluid density | 1000 kg m^{-3} | [47] |
| α | Beavers-Joseph friction parameter | 10^{-3} | Numerical |

flow-mediated angiogenesis where we explore the impact of flow on angiogenesis.

4.1 Flow model validation through a manufactured solution

Due to the complex nature of the coupled Stokes–Darcy problem, we use the method of manufactured solutions to validate our numerical formulation for the diffuse-interface approximation of the Stokes–Darcy problem. We define a sharp-interface Stokes–Darcy problem (Definition 3) with known solution by imposing appropriate body forces and boundary conditions. We consider a rectangular domain $\Omega = (0,\pi) \times (-1,1)$, where the Stokes domain is $\Omega_S = (0,\pi) \times (0,1)$, the Darcy domain is $\Omega_D = (0,\pi) \times (-1,0)$, and the interface is $\Gamma = (0,\pi) \times \{0\}$. For simplicity, the Stokes and Darcy domains are time-independent. The exact solution of the manufactured problem, $(u_S, p_S, p_D) \in H^1(\Omega_S) \times L^2(\Omega_S) \times H^1(\Omega_D)$, is expressed as

$$u_{S}(x,y) = \begin{bmatrix} \frac{\mathrm{d}w(y)}{\mathrm{d}y} \cos(x) \\ w(y) \sin(x) \end{bmatrix},$$
with $w(y) = -K - \frac{gy}{2\nu} + \left(\frac{K}{2} - \frac{\alpha g}{4\nu^{2}}\right)y^{2},$

$$(47)$$

$$p_S(x, y) = p_{S0}, (48)$$

$$p_D(x, y) = \rho g \exp(y) \sin(x) + \rho p_{S0}, \tag{49}$$

where *K* is the hydraulic conductivity defined as $K = \frac{k\rho g}{\mu}$, *g* is the acceleration due to gravity, p_{50} is a constant, and the rest of the parameters are introduced in Sect. 2.2. This solution results from setting the parameters values k = 1 and $\nu = 1$ in the governing equations and imposing the manufactured body force [56, 57]:

$$\boldsymbol{b}(x,y) = \begin{bmatrix} \left[-\frac{g}{2} + \left(\nu K - \frac{\alpha g}{2\nu} \right) y \right] \cos(x) \\ \left[\frac{\alpha g}{2\nu} - 2\nu K - \frac{g}{2}y + \left(\frac{\nu K}{2} - \frac{\alpha g}{4\nu} \right) y^2 \right] \sin(x) \end{bmatrix}. \tag{50}$$

We solve the diffuse-interface approximation of the Stokes–Darcy manufactured problem using the numerical algorithm described in the previous sections. We consider a phase field c that is time-independent, with c=1 in Ω_S and c=-1 in Ω_D . We compute c using the 1D steady state solution to the Cahn–Hilliard equation, as shown in [18]. The phase field c is defined as

$$c = \tanh\left(\frac{y}{\epsilon}\right),\tag{51}$$



where the interface width ϵ depends on the mesh, such that $\epsilon = h_{\text{max}}$, where h_{max} is the maximum size of the mesh elements. We set the parameter values g = 1, $\alpha = 1$, $\rho = 1$, and $p_{s0} = 1$. We set Dirichlet boundary conditions on the entire boundary. The top, left and right edges comprise the extended Stokes boundary $\partial \Omega_{S1}^e$ and the bottom, left, and right edges comprise the extended Darcy boundary $\partial \Omega_{D_1}^e$. We obtain $u_{\rm g}^{\epsilon}$ (respectively, $p_{\rm p}^{\epsilon}$) by evaluating the manufactured solution (Eqs. (47)–(49)) on $\partial \Omega_{S,1}$ (respectively, $\partial \Omega_{D,1}$) and constantly extending the interfacial value along the edge defined by $\partial \Omega_{S,2}^e \cap \Omega_D$ (respectively, $\partial \Omega_{D,1}^e \cap \Omega_S$). We solve the diffuse-interface approximation (Eq. (45)) of the manufactured problem using a uniform triangular mesh with mesh size h_m . We show the simulation results for $h_m = 0.012$ in Fig. 3, where we plotted the multiphysics velocity u on the left and the multiphysics pressure p on the right.

To study the convergence of our numerical algorithm, we run simulations with decreasing mesh size h_m . To validate the performance of our algorithm, we need to compare the numerical solution, namely $(\boldsymbol{u}_S^{\varepsilon,h}, p_S^{\varepsilon,h}, p_D^{\varepsilon,h})$, with the exact solution to the diffuse-interface approximation of the manufactured problem, namely $(\boldsymbol{u}_S^{\varepsilon}, p_S^{\varepsilon}, p_D^{\varepsilon})$. Since we do not know $(\boldsymbol{u}_S^{\varepsilon}, p_S^{\varepsilon}, p_D^{\varepsilon})$, we instead estimate the numerical error using an error norm based on weighted Lebesgue spaces (see Eq. 31) to compare the numerical solution with the exact solution of the manufactured problem. The relative error norms of the Stokes–Darcy unknowns are defined below

$$e_{u_S} = \frac{\|u_S^{\epsilon,h} - u_S\|_{L^2(\Omega_S, \phi)}}{\|u_S\|_{L^2(\Omega_S)}},$$
(52)

$$e_{p_S} = \frac{\|p_S^{\epsilon,h} - p_S\|_{L^2(\Omega_S, \phi)}}{\|p_S\|_{L^2(\Omega_S)}},$$
(53)

$$e_{p_D} = \frac{\|p_D^{\epsilon,h} - p_D\|_{L^2(\Omega_D, 1-\phi)}}{\|p_D\|_{L^2(\Omega_D)}},$$
(54)

where (u_S, p_S, p_D) is the exact solution of the manufactured problem. We show the convergence of our numerical algorithm for the Stokes–Darcy problem in Fig. 4. The figure shows the errors e_{u_S} , e_{p_S} and e_{p_D} , which decrease with decreasing mesh size h_{max} . Note that the interface width ϵ decreases at the same rate as the mesh size h_{max} . We observe that the convergence rates are in good agreement with theoretical convergence rates [31].

4.2 Prominent vasculature growth against the flow

In this section, we demonstrate the effect of flow on angiogenesis. To do that, we simulate a scenario similar to the experiment carried out in [4]. In this experiment, capillaries grow within an in-vitro microfluidic platform that simultaneously controls interstitial flow and TAF concentration. The experiment shows that the vascular network grows more prominently against the direction of the interstitial flow.

Here, we consider three different cases, namely, inflow, outflow, and control. Figure 5 shows the geometry and the flow model boundary conditions associated with the control, inflow, and outflow simulations. The control case corresponds to angiogenesis with no flow (Fig. 6). The

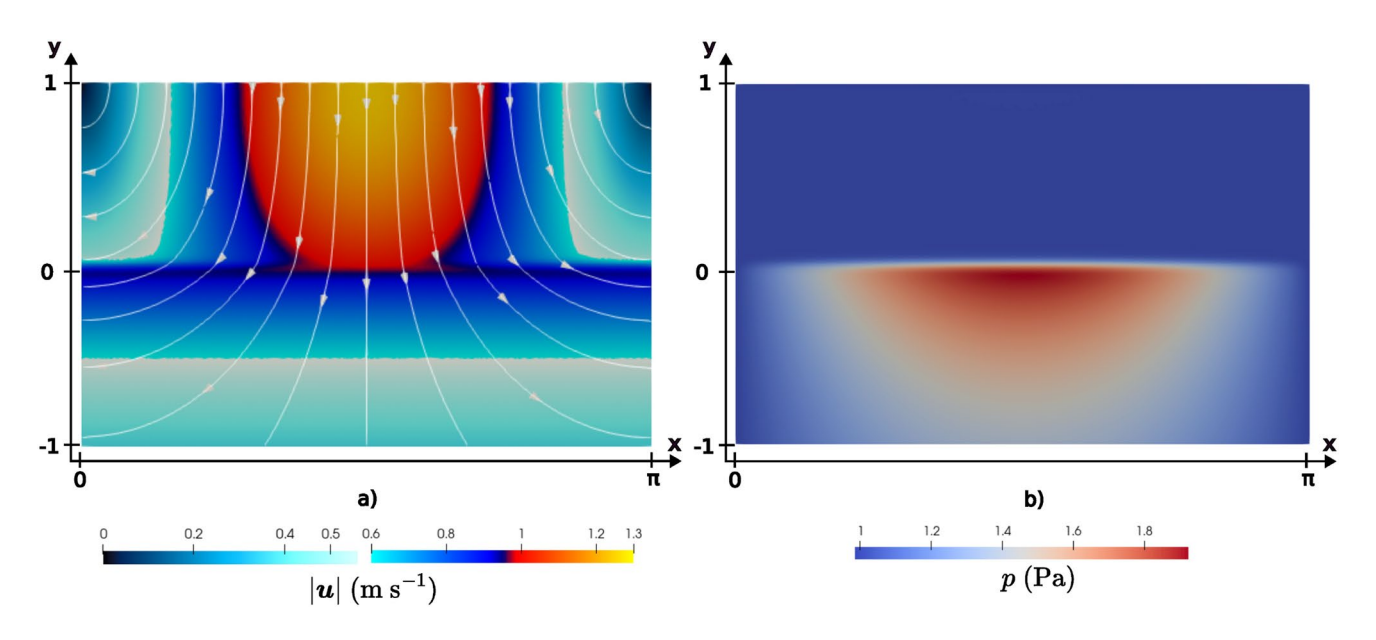
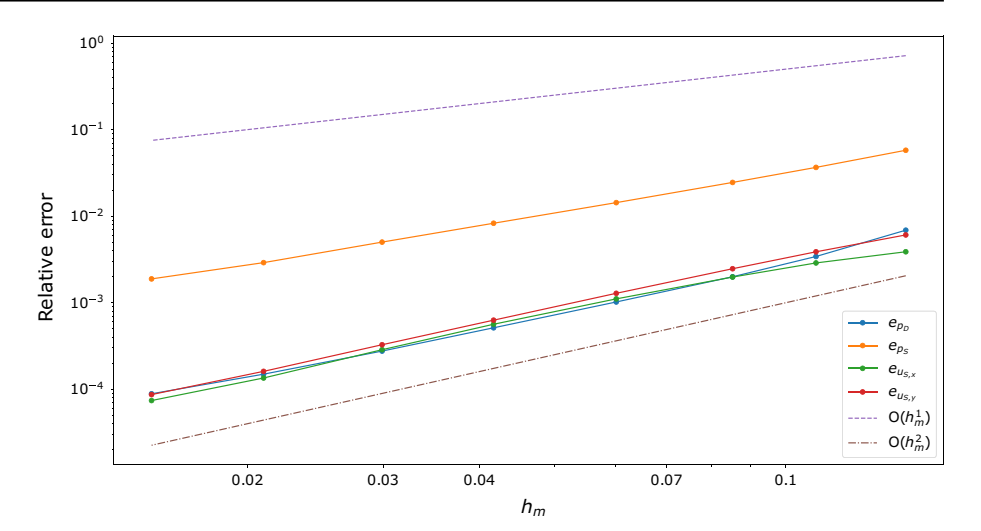


Fig. 3 Manufactured Stokes-Darcy problem: Simulation results using a triangular mesh with element size $h_m = 0.012$. a Magnitude of the multiphysics velocity |u| with overlaid white streamlines. The arrows indicate the direction of u. b Distribution of the multiphysics pressure p



Fig. 4 Manufactured Stokes—Darcy problem: Convergence of the relative error defined in Eqs. (52), (53), and (54) for the Stokes velocity, Stokes pressure, and Darcy pressure. The solid lines with circular markers are log–log plots of the error norm with decreasing mesh size h_m . The circular markers denote the error norm values obtained from the simulation results. The dashed lines represent reference trends of a first- and second-order accurate algorithm



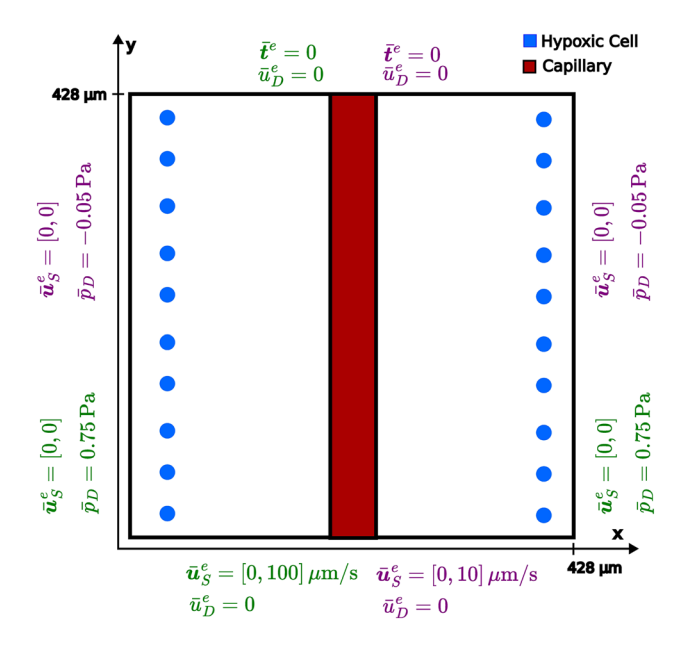
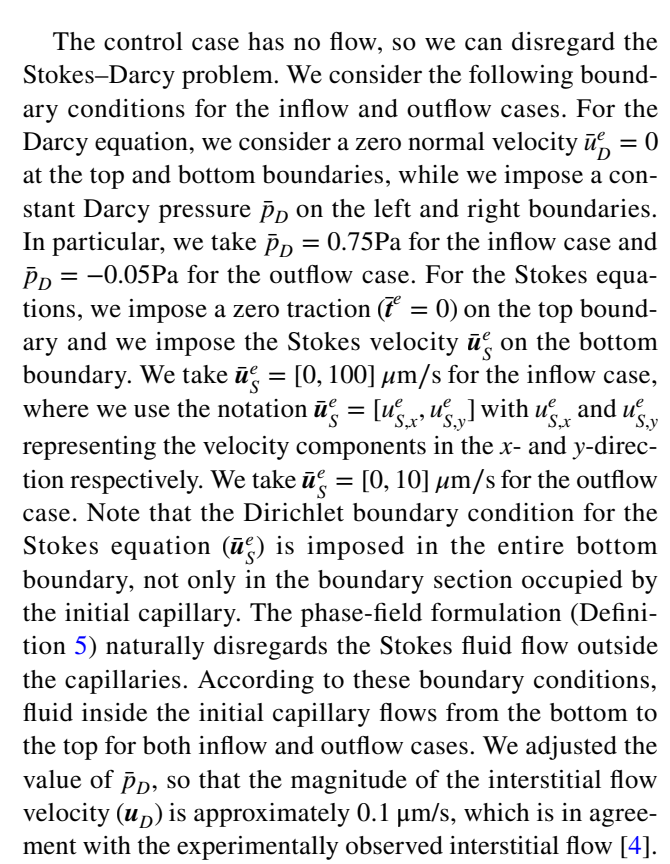


Fig. 5 Geometry and boundary conditions for the control, inflow, and outflow simulations: The initial capillary placement and the location of the hypoxic cells are indicated in red and blue color, respectively. The flow model boundary conditions for the inflow and outflow cases are shown in green and purple color, respectively (color figure online)

inflow case represents a vein that is at a lower pressure than the interstitium. Hence, fluid flows from the interstitium into the vein (Fig. 7). The outflow case represents an artery that is at a higher pressure than the interstitium and, hence, fluid flows from the artery to the interstitium (Fig. 8). To simulate the three cases, we consider a square domain Ω of size $428 \times 428 \,\mu\text{m}$. We initially consider a 20 μm -wide vertical capillary at the center of the domain and hypoxic cells at the left and right sides of the domain, as shown in Fig. 5.



The transport of TAF in the control case simulation is facilitated by diffusion only. Figure 6 shows the effect of diffusive transport on the TAF distribution and the resulting vasculature. We observe the length of new capillaries protruding from the initial capillary is approximately equal in the control case.

The inflow case unveils the underlying biophysics of flow-mediated angiogenesis. We show the simulation results of the inflow case in Fig. 7, where we plot the TAF distribution and vascular geometry (top row), the



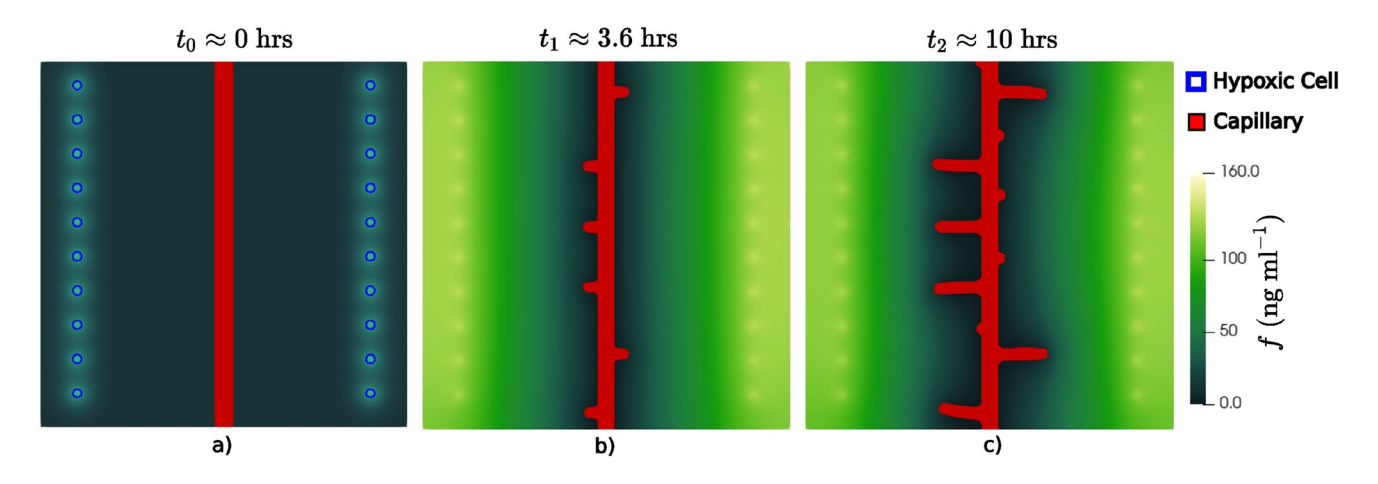


Fig. 6 Control case: The simulation shows vascular growth in the absence of interstitial flow. Time evolution of the TAF distribution and the vascular network at times $\mathbf{a} \ t_0 \approx 0\mathbf{h}, \ \mathbf{b} \ t_1 \approx 3.6\mathbf{h}$, and

 \mathbf{c} $t_2 \approx 10 \mathrm{h}$. The red region represents the vascular network. The hypoxic cells are marked with a blue outline in \mathbf{a} (color figure online)

multiphysics velocity u (middle row), and the multiphysics pressure p (bottom row). Note that the magnitude of the intravascular flow is significantly larger than the magnitude of the interstitial flow. Due to this reason, we have employed a nonlinear color scale to visualize u in Fig. 7d-f. The nonlinear color scale combines two linear scales to separately capture the variation of u in extravascular and intravascular regions. Figure 7d shows u at initial time t_0 . We observe interstitial flow from the left and right boundaries merging into the initial capillary (see arrows in Fig. 7d). At time $t_1 \approx 3.6$ h, multiple TECs have been activated, creating new branches from the main capillary (Fig. 7b). Compared to t_0 , the multiphysics velocity \boldsymbol{u} at t_1 is no longer a pure inflow pattern due to the presence of new capillaries (compare Fig. 7d and e). The sprouting of the new branches increases the pressure around the bottom of the initial capillary (Fig. 7h and i), which causes localized outflow from the initial capillary to the interstitium.

Figure 7a–c showcases the combined effect of TAF advection and diffusion in the inflow case. Upon comparing with the control case (Fig. 6), we observe increased TAF concentration in the regions of high inflow velocity for the inflow case (compare Figs. 6b and 7b). At time $t_2 \approx 10$ h, we observe that the new capillaries have significantly altered the interstitial flow pattern (Fig. 7f). The final geometry of the vascular network in the inflow simulation is different from the control simulation (compare Figs. 6c and 7c). These observations underscore the complex coupling between the vascular network geometry and the interstitial flow.

We plot the simulation results of the outflow case in Fig. 8. The inflow, outflow, and control case simulations display different rates of vascular growth. At the final time of the simulation ($t_2 \approx 10$ h), the inflow case displays larger new capillaries than the control case, and the control case

displays larger new capillaries than the outflow case (compare Figs. 6c, 7c, and 8c). This trend is in agreement with experiments [4]. Preferential capillary growth against the flow is caused by the advective transport of TAF. Advective transport of TAF toward the initial capillary is higher for the inflow case. Thus, TAF arrives earlier at the initial capillary, which provokes a faster TEC activation for the inflow case. The results also show that TAF gradients at the TECs are higher for the inflow case, which leads to larger TEC velocities (see Eq. (11)). These two mechanisms combined produce larger branches for the inflow case. The opposite effects are observed for the outflow case.

4.3 Interstitial flow enhances vasculature growth in a magnitude-dependent manner

In this section, we simulate a scenario similar to the experiments performed in [3] where they investigated the effect of interstitial flow and TAF concentration on micro-vascular network formation. These experiments were conducted using an in-vitro microfluidic device. The experiment showed that the growth of the vascular network increases with increasing interstitial flow magnitude.

Our goal is to reproduce this experimental observation by simulating flow-mediated angiogenesis in three different cases, where we impose different inflow Darcy velocities. We perform the simulations on a $428 \times 428 \,\mu\text{m}$ domain and place the initial capillary near the left edge of the domain (see Fig. 9a). We place ten equally spaced hypoxic cells near the right edge of the domain as shown in Fig. 10a. Unless otherwise stated, the parameter values used in this section are listed in Table 1. We modify the TAF threshold for TEC activation to raccommodate for the increased distance between the capillary and the hypoxic



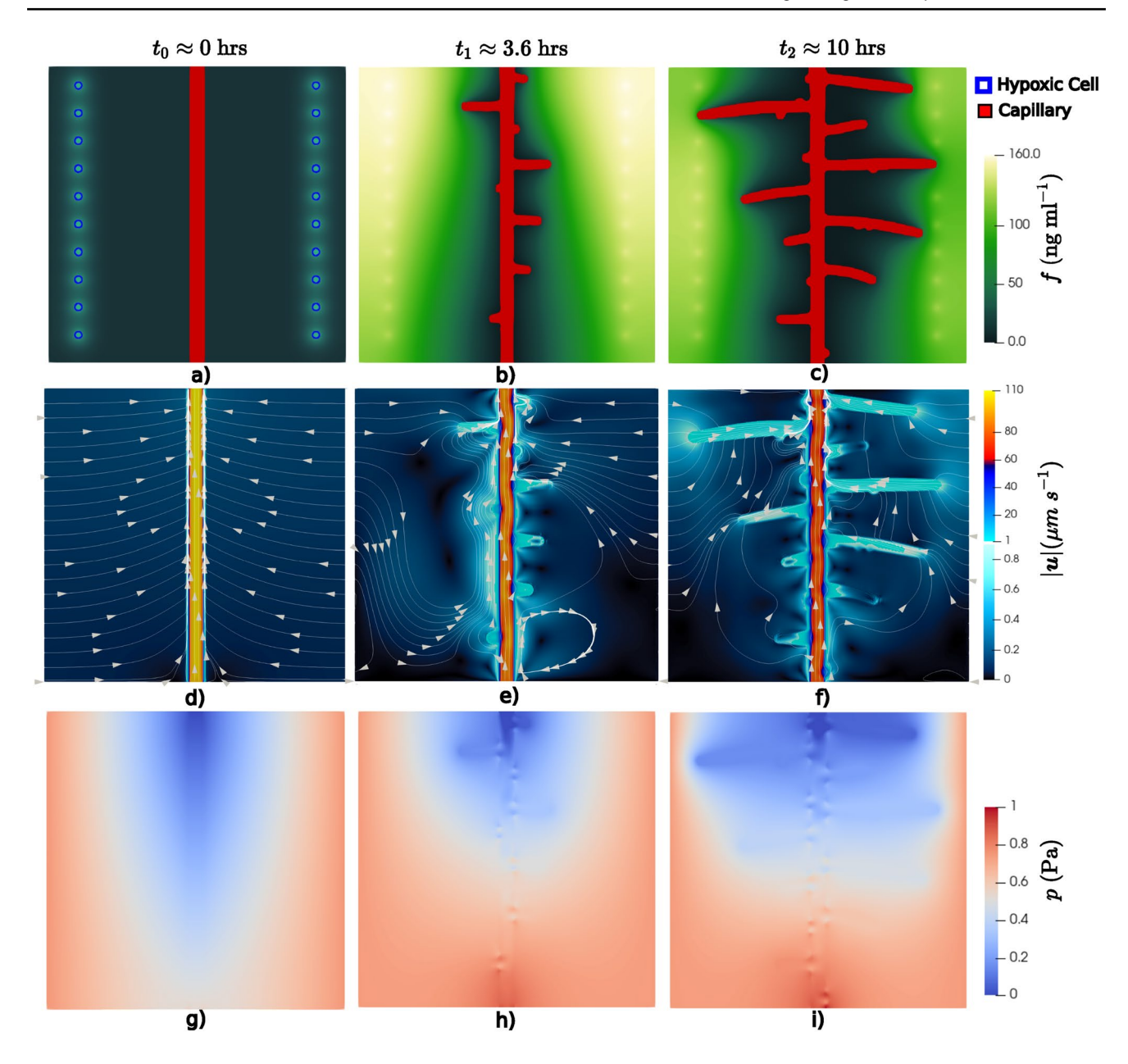


Fig. 7 Inflow case: The simulation shows vascular growth when fluid flows from the interstitium into the capillary. Capillary growth is more prominent against the flow. Time evolution of the **a–c** TAF distribution and capillary network, **d–f** magnitude of multiphysics veloc-

ity |u|, and g-i multiphysics pressure p at times $t_0 \approx 0$ h, $t_1 \approx 3.6$ h, and $t_2 \approx 10$ h. White lines in d-f represent streamlines of u and the arrows indicate the direction of u. The hypoxic cells are marked with a blue outline in a (color figure online)

cells [15], such that $f_{act}=0.18$ ng/ml. For the Stokes problem, we consider analogous boundary conditions as in the previous section, i.e., zero traction on the top boundary and a fixed inflow Stokes velocity $\bar{u}_S^e=[0,10]~\mu m~s^{-1}$ on the entire bottom boundary. For the Darcy problem, we consider a zero normal Darcy velocity on the bottom, top, and left boundaries. On the right boundary, we impose a fixed inflow normal Darcy velocity \bar{u}_D . To analyze the effect of the interstitial flow magnitude on angiogenesis, we run three simulations with different values of \bar{u}_D . In

particular, we consider low ($\bar{u}_D=-0.05~\mu\text{m/s}$), medium ($\bar{u}_D=-0.075~\mu\text{m/s}$), and high ($\bar{u}_D=-0.1~\mu\text{m/s}$) Darcy velocity.

We plot the simulation results in Fig. 9, where the normal Darcy velocity \bar{u}_D increases from bottom to top rows. The results show that the length of the new capillaries at the final time ($t_2 \approx 11.5 \, \text{h}$) increases as \bar{u}_D increases. Thus, vascular growth is more prominent for higher interstitial flow magnitude, which is in qualitative agreement with experiments [3].



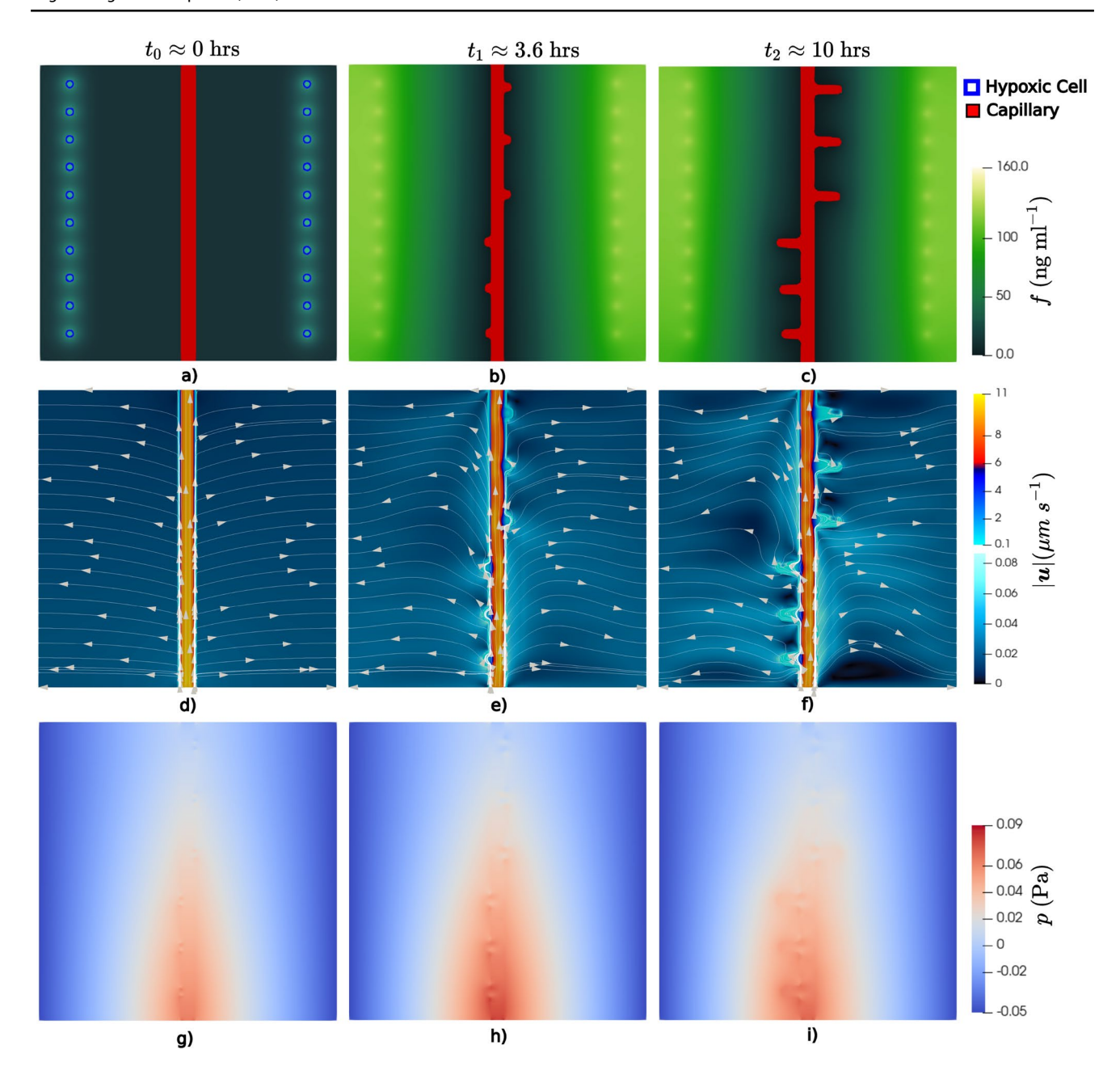


Fig. 8 Outflow case: The simulation shows vascular growth when fluid flows from the capillary network into the intertitium. Time evolution of the \mathbf{a} - \mathbf{c} TAF distribution and capillary network, \mathbf{d} - \mathbf{f} magnitude of multiphysics velocity $|\mathbf{u}|$, and $(\mathbf{g}$ - $\mathbf{i})$ multiphysics pressure

p at times $t_0 \approx 0$ h, $t_1 \approx 3.6$ h, and $t_2 \approx 10$ h. White lines in **d-f** represent streamlines of \boldsymbol{u} and the arrows indicate the direction of \boldsymbol{u} . The hypoxic cells are marked with a blue outline in \boldsymbol{a} (color figure online)

We explain this behavior by comparing the growth of the upper capillary for high and low \bar{u}_D (top and bottom rows, respectively, in Fig. 9). Figure 10 shows the evolution of TAF concentration with time for high \bar{u}_D . We note that the results shown in Fig. 10 are indicative of the trend of TAF distribution exhibited by medium and low \bar{u}_D and we will utilize the trend of TAF distribution shown in Fig. 10 to detail our reasoning.

First, we denote the center of the TEC driving the growth of the upper capillary as x_T , the magnitude of the TAF gradient at x_T as $|\nabla f|_T$, the magnitude of the multiphysics velocity at x_T as u_T , and the distance between x_T and the closest hypoxic cell as d_T . The vascular growth rate of the new capillaries is proportional to $|\nabla f|_T$ (see Eq. (11)), which increases with (1) increasing u_T and (2) decreasing d_T . Since TAF uptake by the vascular network is high, we observe that the TAF concentration at x_T is close to zero.



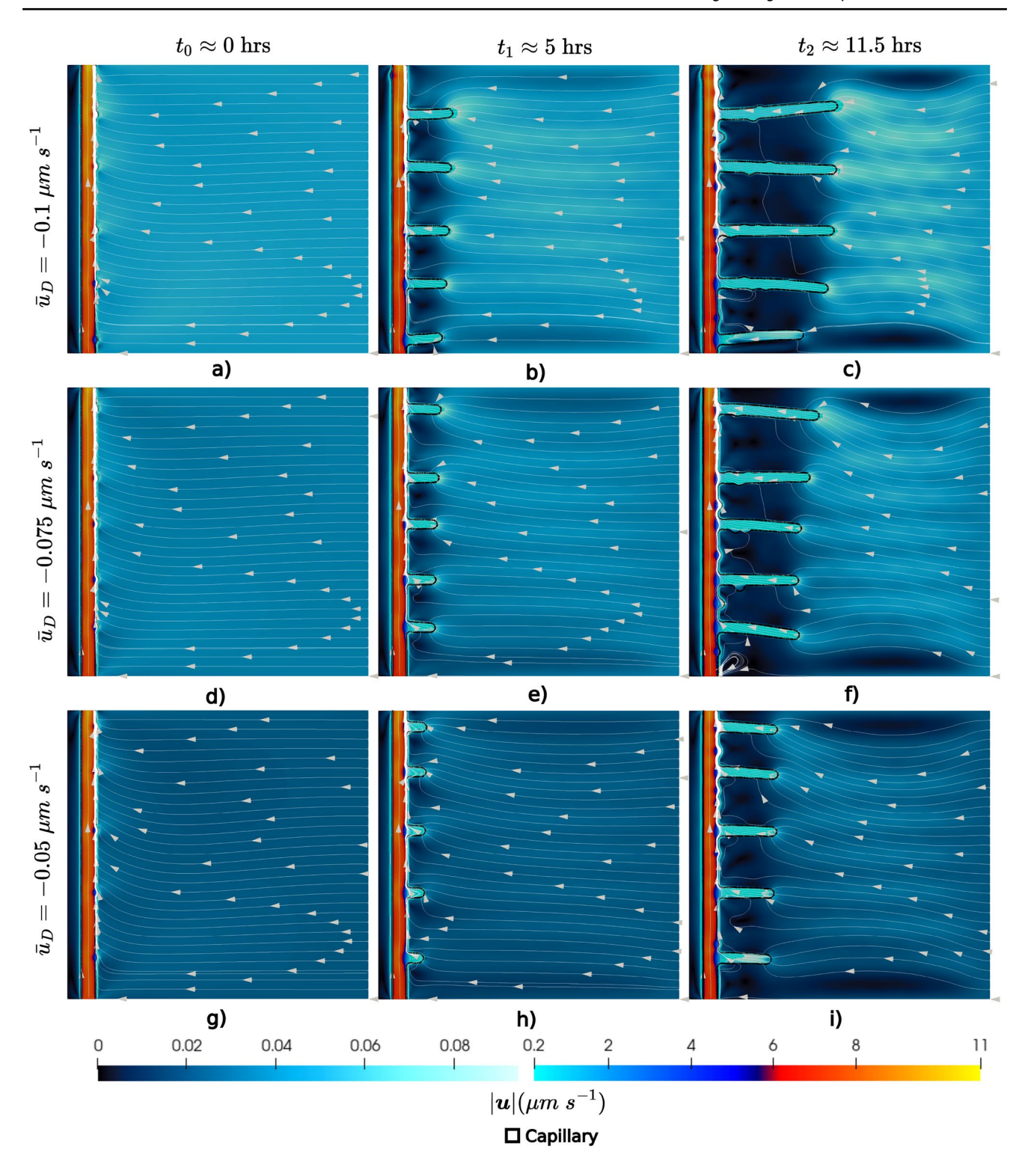


Fig. 9 Effect of the interstitial flow magnitude on vascular growth. Simulation results for the boundary interstitial fluid flow \bar{u}_D =-0.1 (**a**-**c**), -0.075 (**d**-**f**), and -0.05 μ m/s (**g**-**i**) at times $t_0 \approx 0$ h (left column), $t_1 \approx 5$ h (center column), and $t_2 \approx 11.5$ h (right column). The figure

shows the magnitude of the multiphysics velocity u, where the white lines are streamlines of u and arrows indicate the velocity direction. The black contour line represents the outline of the capillary network (color figure online)



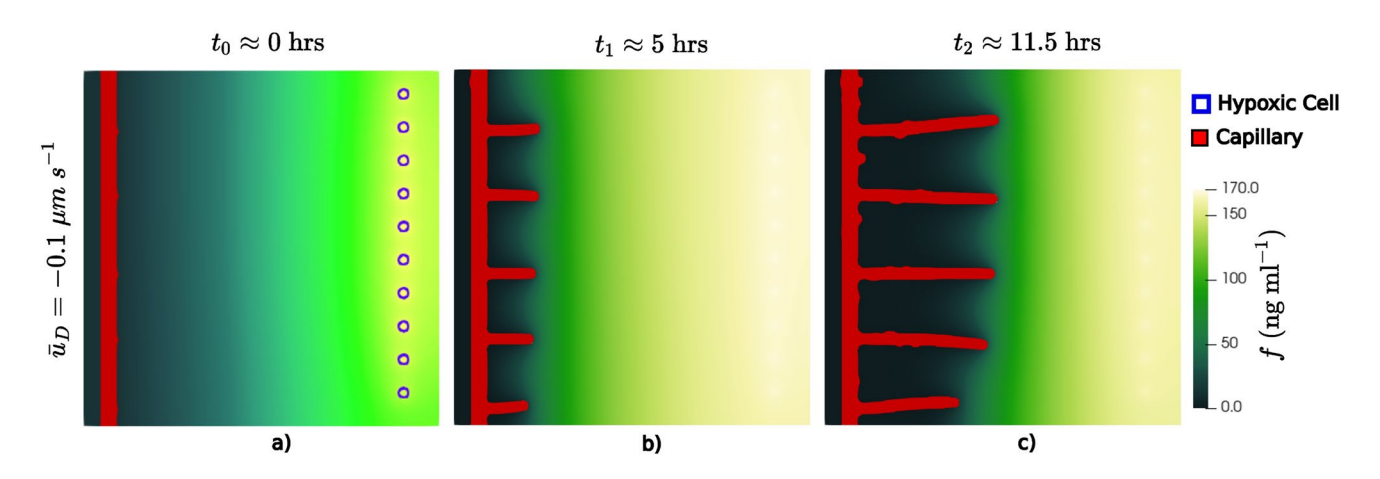


Fig. 10 Effect of the interstitial flow magnitude on vascular growth. Simulation results for inflow normal Darcy velocity at the boundary $\bar{u}_D = -0.1 \ \mu \text{m/s}$. a-c shows the time evolution of TAF distribution at

times $t_0 \approx 0$ h (**a**), $t_1 \approx 5$ h (**b**) and $t_2 \approx 11.5$ h (**c**). The hypoxic cells are marked with a blue outline in **a** (color figure online)

Thus, the TAF gradient inside the TEC is proportional to the TAF concentration at the border of the TEC, which increases with higher advective transport, i.e., higher u_T . Likewise, we observe that the TAF concentration at the hypoxic cell is $f_{\rm HYC}$ and has a quasi-linear distribution between the TEC and the hypoxic cell. Hence, the TAF gradient between those two cells and $|\nabla f|_T$ increase as the distance d_T decreases. Thus, capillary growth is faster as \bar{u}_D increases and TECs get closer to the hypoxic cells. This behavior persists until TECs reach the maximum speed determined by G_M (see Eq. (11)).

We observe this behavior in Fig. 9. At the initial time (t_0) , u_T is higher for higher \bar{u}_D , while d_T is the same in the three simulations. Thus, new capillaries grow faster for higher \bar{u}_D (top row in Fig. 9) due to higher u_T . As the simulation evolves, the distance d_T decreases faster for larger \bar{u}_D (compare Fig. 9b and e), which provokes a positive feedback that accelerates vascular growth for higher \bar{u}_D . These two combined factors provoke a faster capillary growth for higher interstitial flow (compare Fig. 9c, f, and i) as long as TAF gradients are below the limit G_M for maximum TEC speed.

5 Conclusion

The impact of intravascular and interstitial flow on tumor angiogenesis is not well understood. Several experiments have suggested that shear stress and flow velocity affect crucial events in angiogenesis, such as the TEC sprouting location, TEC velocity, and anastomosis. The design of experiments in flow-controlled and TAF-controlled conditions to study flow-mediated angiogenesis is challenging. *In silico* investigation bypasses some of the experimental challenges and has the potential to unveil the tight interplay between capillary growth and vascular flow in some scenarios. However, previous modeling efforts resorted to

simplified flow models to reproduce intra- and extravascular flow on changing capillary geometries [11-13, 58]. In this work, we develop a computational model of flow-mediated angiogenesis which accurately predicts flow on temporally evolving vascular networks. Our model couples the angiogenesis model proposed in [15] with the Stokes-Darcy flow equations and uses the phase-field method to capture the time-evolving geometry of the vessels. Built on the phasefield method, we derive a diffuse-interface formulation for both the angiogenesis and the Stokes-Darcy equations which avoids the computational cost of re-meshing, as opposed to other sharp-interface methods. We demonstrate the validity of the flow model by comparing the numerical solution to a manufactured test case. We find that the convergence rate of the weighted error norm of the solution is in good agreement with theoretical results.

Our modeling framework successfully reproduces intraand extravascular flow on growing vascular networks. Our
simulation results show that the convective transport of TAF
has a significant impact on the shape of the vasculature.
Thus, our model offers a fluid-dynamics explanation for the
prominent growth of vasculature against the flow direction
observed in experiments in [4]. Further, our model predicts
enhanced vasculature growth with increasing interstitial
flow magnitude, which was observed experimentally in [3].
Our results suggest that the dominant mechanism behind
the observed trend is the dependence of TEC velocity magnitude on the TAF gradient. The simulations indicate that
higher interstitial flow leads to an increased TAF gradient
at the TEC, which causes the observed trend.

In future work, we plan to integrate various flow-based biophysical cues into our modeling framework and investigate their effect on angiogenesis [3–10]. We are particularly interested in the effect of shear stress on the capillary sprouting location [6, 8, 10]. We believe that the coupling between



the sprouting mechanism, the fluid flow, and the vasculature growth will yield interesting insights into the biophysics of tumor angiogenesis. Our model can be further improved in several ways. For instance, the model can be extended with the evolution equations for the nutrients and oxygen that control the irrigation of the hypoxic cells, as shown in [59]. This would lead to a more accurate representation of the TAF-production decay of the hypoxic cells. Another possible improvement to the intravascular model is to include the shear thinning behavior of blood.

Acknowledgements This work was partially supported by the National Science Foundation under (Award No. CMMI 1852285). The opinions, findings, and conclusions, or recommendations expressed are those of the authors and do not necessarily reflect the views of the National Science Foundation.

Data Availability Data will be made available on request.

Declarations

Conflict of interest The authors have no competing interests to declare that are relevant to the content of this article.

References

- Folkman J (1971) Tumor angiogenesis: therapeutic implications. N Engl J Med 285(21):1182–1186
- Carmeliet P, Jain RK (2000) Angiogenesis in cancer and other diseases. Nature 407(6801):249–257
- Abe Y, Watanabe M, Chung S, Kamm RD, Tanishita K, Sudo R (2019) Balance of interstitial flow magnitude and vascular endothelial growth factor concentration modulates three-dimensional microvascular network formation. APL Bioeng 3(3):036102
- Shirure VS, Lezia A, Tao A, Alonzo LF, George SC (2017) Low levels of physiological interstitial flow eliminate morphogen gradients and guide angiogenesis. Angiogenesis 20:493–504
- Kim S, Chung M, Ahn J, Lee S, Jeon NL (2016) Interstitial flow regulates the angiogenic response and phenotype of endothelial cells in a 3D culture model. Lab Chip 16(21):4189–4199
- Galie PA, Nguyen D-HT, Choi CK, Cohen DM, Janmey PA, Chen CS (2014) Fluid shear stress threshold regulates angiogenic sprouting. Proc Natl Acad Sci 111(22):7968–7973
- Akbari E, Spychalski GB, Rangharajan KK, Prakash S, Song JW (2019) Competing fluid forces control endothelial sprouting in a 3-D microfluidic vessel bifurcation model. Micromachines 10(7):451
- Ghaffari S, Leask RL, Jones EA (2015) Flow dynamics control the location of sprouting and direct elongation during developmental angiogenesis. Development 142(23):4151–4157
- Udan RS, Vadakkan TJ, Dickinson ME (2013) Dynamic responses of endothelial cells to changes in blood flow during vascular remodeling of the mouse yolk sac. Development 140(19):4041–4050
- Song JW, Munn LL (2011) Fluid forces control endothelial sprouting. Proc Natl Acad Sci 108(37):15342–15347
- Moure A, Vilanova G, Gomez H (2022) Inverting angiogenesis with interstitial flow and chemokine matrix-binding affinity. Sci Rep 12(1):4237
- McDougall SR, Anderson AR, Chaplain MA (2006) Mathematical modelling of dynamic adaptive tumour-induced angiogenesis:

- clinical implications and therapeutic targeting strategies. J Theor Biol 241(3):564–589
- Vilanova G, Burés M, Colominas I, Gomez H (2018) Computational modelling suggests complex interactions between interstitial flow and tumour angiogenesis. J R Soc Interface 15(146):20180415
- Pradelli F, Minervini G, Tosatto SC (2022) Mocafe: a comprehensive python library for simulating cancer development with phase field models. Bioinformatics 38(18):4440–4441
- Travasso R, Corvera E, Castro Ponce M, Rodríguez-Manzaneque J, Rodrguez-Manzaneque J, Hernández-Machado A (2011) Tumor angiogenesis and vascular patterning: a mathematical model. PLoS ONE 6:19989
- Bazilevs Y, Takizawa K, Tezduyar TE (2013) Computational fluid-structure interaction: methods and applications. John Wiley and Sons, New Jersey
- Discacciati M, Quarteroni A et al (2009) Navier-Stokes/Darcy coupling: modeling, analysis, and numerical approximation. Rev Mat Complut 22(2):315–426
- Gomez H, Zee KG (2018) Computational phase-field modeling. Encyclopedia of computational mechanics, 2nd edn. Wiley, New Jersey, pp 1–35
- Gomez H, Bures M, Moure A (2019) A review on computational modelling of phase-transition problems. Phil Trans R Soc A 377(2143):20180203
- Bures M, Moure A, Gomez H (2021) Computational treatment of interface dynamics via phase-field modeling. Numerical simulation in physics and engineering: trends and applications: lecture notes of the XVIII 'Jacques-Louis Lions' Spanish-French school. Springer, Cham, pp 81–118
- Wells GN, Kuhl E, Garikipati K (2006) A discontinuous Galerkin method for the Cahn-Hilliard equation. J Comput Phys 218(2):860–877
- Wu H (2021) A review on the cahn-hilliard equation: classical results and recent advances in dynamic boundary conditions. arXiv preprint arXiv:2112.13812
- Hellström M, Phng L-K, Hofmann JJ, Wallgard E, Coultas L, Lindblom P, Alva J, Nilsson A-K, Karlsson L, Gaiano N et al (2007) Dll4 signalling through notch1 regulates formation of tip cells during angiogenesis. Nature 445(7129):776–780
- Vilanova G, Colominas I, Gomez H (2013) Capillary networks in tumor angiogenesis: From discrete endothelial cells to phasefield averaged descriptions via isogeometric analysis. Int J Numer Methods Biomed Eng 29(10):1015–1037
- Vilanova G, Colominas I, Gomez H (2017) Computational modeling of tumor-induced angiogenesis. Arch Comput Methods Eng 24(4):1071–1102
- Evans LC (2022) Partial differential equations, vol 19. American Mathematical Society, Providence
- Beavers GS, Joseph DD (1967) Boundary conditions at a naturally permeable wall. J Fluid Mech 30(1):197–207
- Layton WJ, Schieweck F, Yotov I (2002) Coupling fluid flow with porous media flow. SIAM J Numer Anal 40(6):2195–2218
- Payne LE, Straughan B (1998) Analysis of the boundary condition at the interface between a viscous fluid and a porous medium and related modelling questions. J Math Pures et Appl 77(4):317–354
- Nield D (2009) The beavers-joseph boundary condition and related matters: a historical and critical note. Transp Porous Media 78:537–540
- Bukač M, Muha B (2021) Analysis of the diffuse interface method for the stokes-darcy coupled problem. arXiv preprint arXiv:2112. 12831
- Fried E (2006) On the relationship between supplemental balances in two theories for pure interface motion. SIAM J Appl Math 66(4):1130–1149



- 33. Donea J, Huerta A (2003) Finite element methods for flow problems. John Wiley and Sons, New Jersey
- 34. Tezduyar TE (1991) Stabilized finite element formulations for incompressible flow computations. Adv Appl Mech 28:1–44
- Hughes TJ, Cottrell JA, Bazilevs Y (2005) Isogeometric analysis:
 CAD, finite elements, nurbs, exact geometry and mesh refinement.
 Comput Methods Appl Mech Eng 194(39–41):4135–4195
- Gómez H, Calo VM, Bazilevs Y, Hughes TJ (2008) Isogeometric analysis of the Cahn-Hilliard phase-field model. Comput Methods Appl Mech Eng 197(49–50):4333–4352
- Chung J, Hulbert G (1993) A time integration algorithm for structural dynamics with improved numerical dissipation: the generalized-α method. J Appl Mech 60(2):371
- Jansen KE, Whiting CH, Hulbert GM (2000) A generalized-α method for integrating the filtered Navier-Stokes equations with a stabilized finite element method. Comput Methods Appl Mech Eng 190(3–4):305–319
- Saad Y, Schultz MH (1986) Gmres: a generalized minimal residual algorithm for solving nonsymmetric linear systems. SIAM J Sci Stat Comput 7(3):856–869
- Amestoy PR, Duff IS, L'Excellent J-Y, Koster J (2001) A fully asynchronous multifrontal solver using distributed dynamic scheduling. SIAM J Matrix Anal Appl 23(1):15–41
- Logg A, Wells GN (2010) Dolfin: automated finite element computing. ACM Trans Math Softw (TOMS) 37(2):1–28
- Logg A, Mardal K-A, Wells G (2012) Automated solution of differential equations by the finite element method: the FEniCS book, vol 84. Springer, Cham
- Kirby RC (2004) Algorithm 839: fiat, a new paradigm for computing finite element basis functions. ACM Trans Mathl Softw (TOMS) 30(4):502–516
- Kirby RC, Logg A (2006) A compiler for variational forms. ACM Trans Math Softw (TOMS) 32(3):417–444
- Alnæs MS, Logg A, Ølgaard KB, Rognes ME, Wells GN (2014) Unified form language: a domain-specific language for weak formulations of partial differential equations. ACM Trans Math Softw (TOMS) 40(2):1–37
- Alnæs M, Blechta J, Hake J, Johansson A, Kehlet B, Logg A, Richardson C, Ring J, Rognes ME, Wells GN (2015) The fenics project version 1.5. Arch Numer Softw 3(100)
- Swartz MA, Fleury ME (2007) Interstitial flow and its effects in soft tissues. Annu Rev Biomed Eng 9:229–256
- Shiu Y-T, Weiss JA, Hoying JB, Iwamoto MN, Joung IS, Quam CT (2005) The role of mechanical stresses in angiogenesis. Crit Rev Biomed Eng 33(5):431–510

- Schugart RC, Friedman A, Zhao R, Sen CK (2008) Wound angiogenesis as a function of tissue oxygen tension: a mathematical model. Proc Natl Acad Sci 105(7):2628–2633
- Tong S, Yuan F (2008) Dose response of angiogenesis to basic fibroblast growth factor in rat corneal pocket assay: I. Experimental characterizations. Microvasc Res 75(1):10–15
- 51. Tong S, Yuan F (2008) Dose response of angiogenesis to basic fibroblast growth factor in rat corneal pocket assay: II. Numerical simulations. Microvasc Res 75(1):16–24
- Kleinheinz J, Jung S, Wermker K, Fischer C, Joos U (2010)
 Release kinetics of vegf165 from a collagen matrix and structural matrix changes in a circulation model. Head Face Med 6(1):1–7
- Xu J, Vilanova G, Gomez H (2016) A mathematical model coupling tumor growth and angiogenesis. PLoS ONE 11(2):0149422
- Xu J, Vilanova G, Gomez H (2017) Full-scale, three-dimensional simulation of early-stage tumor growth: the onset of malignancy. Comput Methods Appl Mech Eng 314:126–146
- Gebb S, Stevens T (2004) On lung endothelial cell heterogeneity. Microvasc Res 68(1):1–12
- Stoter SK, Müller P, Cicalese L, Tuveri M, Schillinger D, Hughes TJ (2017) A diffuse interface method for the Navier-Stokes/ Darcy equations: Perfusion profile for a patient-specific human liver based on MRI scans. Comput Methods Appl Mech Eng 321:70–102
- Caiazzo A, John V, Wilbrandt U (2014) On classical iterative subdomain methods for the Stokes-Darcy problem. Comput Geosci 18:711–728
- Flores J, Romero AM, Travasso RD, Poire EC (2013) Flow and anastomosis in vascular networks. J Theor Biol 317:257–270
- Moreira-Soares M, Coimbra R, Rebelo L, Carvalho J, DM Travasso R (2018) Angiogenic factors produced by hypoxic cells are a leading driver of anastomoses in sprouting angiogenesis-a computational study. Sci Rep 8(1):1–12

Publisher's Note Springer Nature remains neutral with regard to jurisdictional claims in published maps and institutional affiliations.

Springer Nature or its licensor (e.g. a society or other partner) holds exclusive rights to this article under a publishing agreement with the author(s) or other rightsholder(s); author self-archiving of the accepted manuscript version of this article is solely governed by the terms of such publishing agreement and applicable law.

